Journal of Asian Earth Sciences 300 (2026) 106990

Contents lists available at ScienceDirect

Journal of Asian Earth Sciences

journal homepage: www.elsevier.com/locate/jseaes

Full length article

Geochemical constraints on the evolution and tectonic setting of United Arab Emirates Ophiolitic Serpentinites

Mabrouk Sami [a,*], Hamed Gamaleldien [b,*], Theodoros Ntaflos [c], Chun-Feng Li [d], Ioan V. Sanislav [e], Xun Zhao [a], Vandi Dlama Kamaunji [f], Bahaa M. Amin [a], Douaa Fathy [g], Mostafa R. Abukhadra [a], Khaled Abdelfadil [a,h], Suhail S. Alhejji [i]

[a] Geosciences Department, College of Science, United Arab Emirates University, Al Ain, United Arab Emirates
[b] Department of Earth Sciences, College of Engineering and Physical Sciences, Khalifa University, Abu Dhabi, United Arab Emirates
[c] Department of Lithospheric Research, University of Vienna, Althanstrasse 14, Vienna A-1090, Austria
[d] Department of Marine Science, Zhejiang University, Zhoushan 316021, China
[e] College of Science and Engineering, James Cook University, Economic Geology, Townsville, QLD 4811, Australia
[f] School of Earth Sciences, China University of Geosciences, Wuhan, China
[g] Geology Department, Faculty of Science, Minia University, El-Minia 61519, Egypt
[h] Geology Department, Faculty of Science, Sohag University, Sohag 82524, Egypt
[i] Geology and Geophysics Department, College of Science, King Saud University, P.O. Box 16 2455, Riyadh 11451, Saudi Arabia

ARTICLE INFO

Keywords:
Harzburgite-dunite serpentinite
Cr-spinel
Subduction zone
Semail ophiolite, Jabal Mundassah
depleted mantle protolith
Platinum group elements
United Arab Emirates

ABSTRACT

Serpentinites in fore-arc settings provide critical constraints on mantle depletion, redox evolution, and slab–mantle fluid transfer during subduction initiation. In the northern Semail Ophiolite of the United Arab Emirates, serpentinites of the Jabal Mundassah–Malaqet (JMM) are studied using mineral chemistry, whole-rock geochemitry, and platinum-group element (PGEs) compositions to constrain protolith characteristics, melting history, and tectono-magmatic evolution. The rocks comprise massive and foliated serpentinites dominated by intergrown lizardite and antigorite with relict Cr-spinel and altered olivine. The JMM serpentinites are characterized by high MgO (34.9–39.2 wt.%), extremely low Al_2O_3 (0.21–0.92 wt.%) and TiO_2 (0.01–0.03 wt.%), elevated Ni (up to 2462 ppm) and Cr (up to 3143 ppm), and very low high-field-strength element (HFSE) and Th–U contents. These features indicate a highly refractory dunite–harzburgite protolith formed by extensive melt extraction. This interpretation is reinforced by Cr-spinel compositions (Cr# = 0.42–0.48; Mg# = 0.58–0.61) and low total PGE abundances (ΣPGE ≈ 15–35 ppb), which are diagnostic of a strongly depleted, sulfide-exhausted mantle residue. Pronounced depletion in HFSE coupled with diagnostic Nb–Th systematics definitively fingerprints a supra-subduction zone (SSZ) fore-arc tectonic setting. PGE systematics (ΣPGE ≈ 8–26 ppb; modest Pt–Pd enrichment over Os–Ir–Ru; low Pd/Ir=1.18-1.61) record moderate partial melting followed by selective mobilization of PPGEs during serpentinization, preserving a dominantly magmatic signature with a limited metasomatic overprint. We propose the JMM serpentinites originated as a highly depleted mantle residue during intra-oceanic subduction initiation. It was subsequently serpentinized by slab-derived fluids under fore-arc conditions before being tectonically emplaced onto the Arabian margin during Late Cretaceous ophiolite obduction. Relative to the main Semail mantle section, the JMM captures an earlier, less-evolved snapshot of fore-arc development during Late Cretaceous obduction, refining models for Neo-Tethyan subduction initiation and ophiolite assembly.

1. Introduction

Serpentinites represent hydrated segments of the Earth's mantle, formed through the hydration of peridotites (Evans et al., 2013). Serpentinization is a widespread process observed in mid-oceanic ridges (MOR) and supra-subduction zone (SSZ) settings (Deschamps et al., 2013; Scambelluri et al., 2019) (Fig. 1a). Serpentinites from these tectonic environments exhibit distinct geochemical signatures shaped by

* Corresponding author.
E-mail addresses: mabrouksami@uaeu.ac.ae (M. Sami), hamed.gamaleldien@ku.ac.ae (H. Gamaleldien).

https://doi.org/10.1016/j.jseaes.2026.106990
Received 10 June 2025; Received in revised form 1 January 2026; Accepted 4 January 2026
Available online 1 February 2026

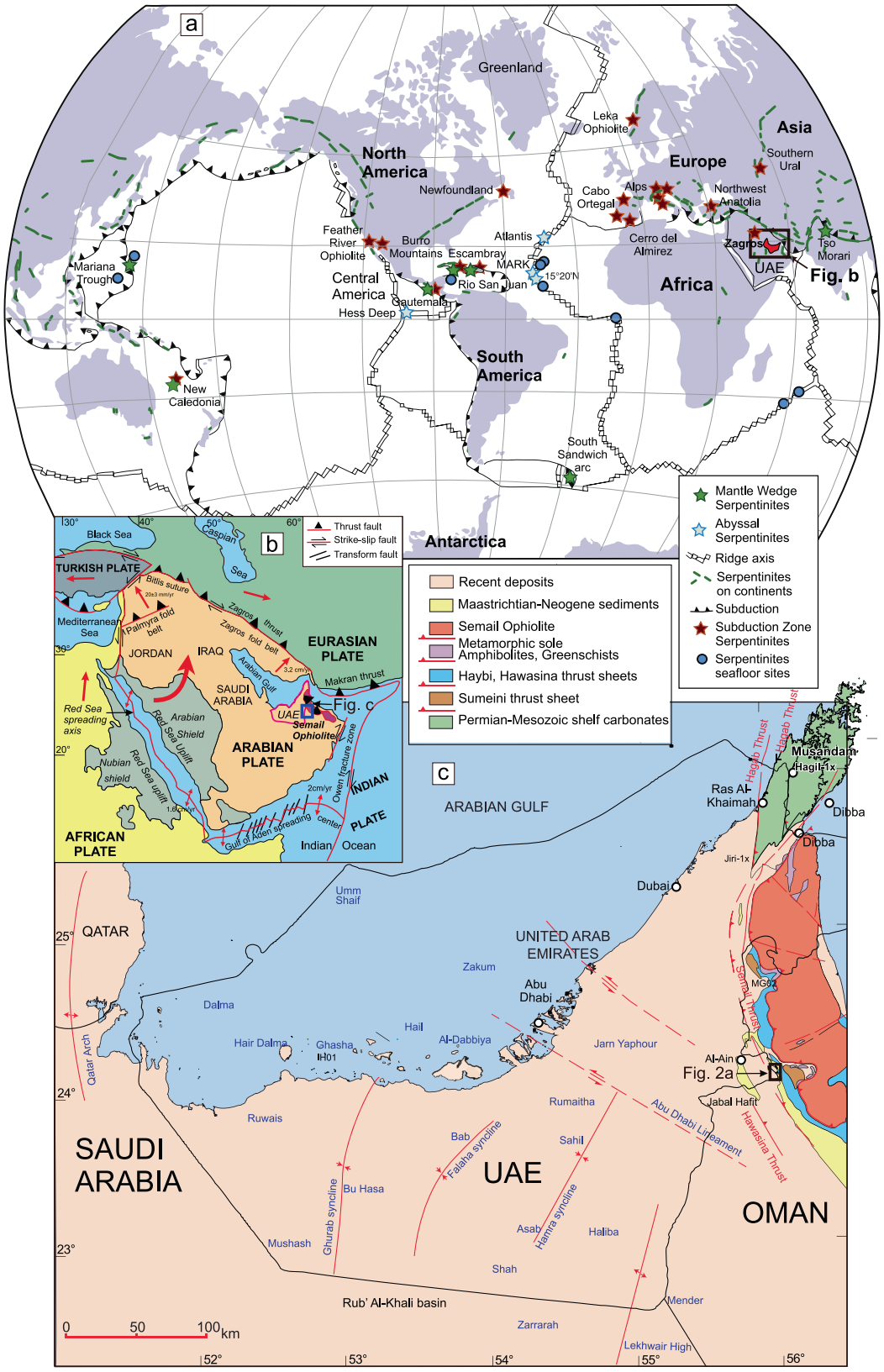

Fig. 1. (a) Worldwide occurrences of serpentinite outcrops and massifs (after Deschamps et al., 2013), (b) Simplified map of the Arabian Plate showing the location of the UAE (after Stern and Johnson, 2010). (c) Simplified geological map of UAE (modified from Saibi et al., 2021).

mantle protolith composition, melt depletion, refertilization, and fluid/melt interaction. These variations are reflected in their whole-rock major and trace element chemistry, as well as in the composition of relict primary minerals such as spinel, and olivine, which are robust tracers of serpentinite tectonic regimes (Deschamps et al., 2013; Ali et al., 2021). Subduction zone serpentinites are increasingly recognized for their critical roles in arc magma chemistry, redox balance regulation, and controlling the oxidation state of fluids released into the mantle during dehydration (Scambelluri et al., 2019). In fore-arc settings, these processes are especially important because slab-derived fluids can strongly modify the oxidation state of the mantle wedge during the earliest stages of subduction (Kelley & Cottrell, 2009; Evans, 2012). Subduction-zone serpentinites are of three types: mantle wedge, abyssal, and subducted serpentinites (Yin et al., 2024). The mantle wedge serpentinites originate from hydrated peridotites in the mantle through fluids from subducted slabs. Abyssal serpentinites form via seawater hydration of oceanic peridotites through seafloor hydrothermal processes. Subducted serpentinites develop as fluids from dehydrating oceanic crust and slab sediments migrate upward into the mantle wedge (Li et al., 2025). Because these serpentinites commonly comprise mixtures of serpentine polymorphs, their mineralogy requires confirmation by crystallographic methods such as XRD or Raman spectroscopy (Beard & Frost, 2017). In particular, fore-arc mantle wedge serpentinites formed during subduction initiation are especially valuable because they record the earliest stages of slab–mantle interaction, extreme melt depletion, and the onset of oxidizing fluid metasomatism (Deschamps et al., 2013; Saha et al., 2018).

In the United Arab Emirates (UAE), serpentinites occur within the northern Semail Ophiolite, one of the world's largest and best-preserved ophiolite complexes (Searle, 2019) (Fig. 1b). In Al-Ain area, they are exposed in the Jabal Mundassah–Malaqet (JMM) anticlines, where sequences of peridotite, serpentinized peridotite, and serpentinite represent dismembered fragments of the ophiolite (El Tokhi et al., 2014) (Fig. 1c). Although the structural and tectonostratigraphic framework of these rocks has been studied (Faris et al., 2012; Abd-Allah et al., 2013), their chemical and mineralogical characteristics remain poorly constrained. In particular, the geochemical signatures of JMM serpentinites and their constituent Cr-spinel and platinum-group elements (PGEs) have received limited attention, despite their significance for constraining mantle source composition, melt evolution, redox state, and fluid–rock interactions (El Tokhi et al., 2014; Eickmann et al., 2021). In particular, whole-rock PGE systematics provide sensitive constraints on sulfide exhaustion, degree of melt extraction, and residual mantle fertility in supra-subduction zone environments (Lorand et al., 2013). However, it remains unclear whether the JMM serpentinites record typical abyssal mantle hydration or instead represent highly depleted fore-arc mantle formed during intra-oceanic subduction initiation. Besides, the serpentine polymorphs in UAE mantle sections have not been previously verified using crystallographic criteria, despite their implications for fluid sources, metamorphic grade, and subduction-related processes.

To resolve these uncertainties, this study integrates new field observations, petrography, serpentine polymorph identification by X-ray diffraction (XRD), whole-rock major and trace element geochemistry, Cr-spinel mineral chemistry, and PGEs systematics for the JMM serpentinites. These datasets are used to (i) constrain the nature and degree of mantle melt depletion recorded by the protolith, (ii) evaluate the redox conditions and extent of slab-derived fluid metasomatism during serpentinization, and (iii) establish the tectonic and geodynamic setting of serpentinite formation within the Neo-Tethyan system. The results provide new constraints on the origin, metasomatic evolution, and fore-arc mantle architecture of the Semail Ophiolite in the eastern UAE.

2. Geological Background and Field Observation

The UAE, located on the northeastern Arabian Plate and bordered by distinct tectonic boundaries, sits on a largely stable plate with minimal internal deformation over the past 2000 Ma (Stern and Johnson, 2010) (Fig. 1b). While much of the UAE is blanketed by Quaternary sediments, bedrock exposures are prominent in the Hajar Mountains, the JMM in the east, and western region of Abu Dhabi (Fig. 1c). These thick successions of Paleozoic–Cenozoic sedimentary deposits rest above deeply buried Precambrian crust (Abd-Allah et al., 2013). The basement exposures are prominent within the Arabian shield, and less so along the Arabia coastline (Jabir et al., 2023). The crust of UAE, with thickness of ~40–45 km belongs to the stable eastern Arabian basement, which has undergone minimal tectonic deformation since ca. 750 Ma, and experienced subsidence and sedimentation that culminated during the Neoproterozoic–Phanerozoic periods (Stern and Johnson, 2010).

The geology of the eastern UAE is dominated by the Late Cretaceous Semail Ophiolite, a fragment of oceanic lithosphere obducted onto the Arabian continental margin during ca. 95–68 Ma (Rioux et al., 2016; Searle, 1999). The Semail Ophiolite is globally significant because it preserves a complete oceanic lithospheric section, from mantle peridotites through crustal gabbros and sheeted dikes to volcanic rocks, making it a key analogue for understanding ophiolite formation and obduction processes (Nicolas et al., 2000; Rollinson, 2017). Its emplacement exerted major control on the tectonic architecture of the Hajar and UAE mountains, leading to flexural deformation, thrust stacking, and foreland basin development.

Serpentinites are a volumetrically important component of the Semail Ophiolite, occurring as altered mantle peridotites (harzburgite, dunite, and lherzolite). In Al-Ain area, these rocks are particularly well-exposed in the Jabal Mundassah–Malaqet (JMM) anticlines, where they represent dismembered fragments of the mantle section. The JMM area is characterized by arcuate post-emplacement folds and thrusts, with a basal ophiolitic mélange overlain unconformably by Tertiary carbonates (El Tokhi et al., 2014) (Fig. 2a). Lithological units include massive and foliated serpentinites, serpentinized peridotites, and minor dunite, prominently exposed in the cores of the JMM anticlines (Abd-Allah et al., 2013).

The JMM serpentinites occur as steeply exposed ultramafic bodies showing distinct textural variations. The massive serpentinites (Fig. 2b) display coarse, blocky structures with minimal foliation, forming rugged outcrops typical of strongly serpentinized peridotites. In contrast, the foliated serpentinites exhibit well-developed planar fabrics and are structurally overlain by Cretaceous–Tertiary carbonate sequences (Fig. 2c). The sharp contact between the serpentinites and the carbonates suggests a tectonic boundary, likely related to post-serpentinization deformation and regional thrusting. Structurally, the JMM serpentinites occur as thrust sheets emplaced prior to and synchronous with folding. They are cut by vertical and horizontal fractures and characterized by foliations, mylonitic fabrics, and NNW–SSE trending folds associated with compressional deformation. The overlying carbonates also record deformation, forming asymmetrical anticline disrupted by thrusts both within the serpentinites and adjacent to the Hawasina mélange (El Tokhi et al., 2014).

This local geology provides the framework for understanding mineralogical and geochemical variations discussed in this study. In addition, the serpentinites of the JMM area share textural and mineralogical similarities with those of the well-documented Oman ophiolite, including mesh-textured serpentine after olivine and bastite after pyroxene. However, the JMM serpentinites are more extensively carbonated and talc-altered, reflecting distinct fluid–rock interaction histories. Comparisons with Oman serpentinites (e.g., those exposed in the Samail Massif) show similar lithological and structural features, particularly in terms of mantle protoliths, deformation fabrics, and serpentinization styles (Godard et al., 2000; Kodolányi et al., 2012). The JMM exposures are more localized, occur within smaller anticlines, and remain less well studied geochemically compared to their Oman counterparts. This highlights the importance of investigating the mineralogical and geochemical records of the JMM serpentinites to better understand their

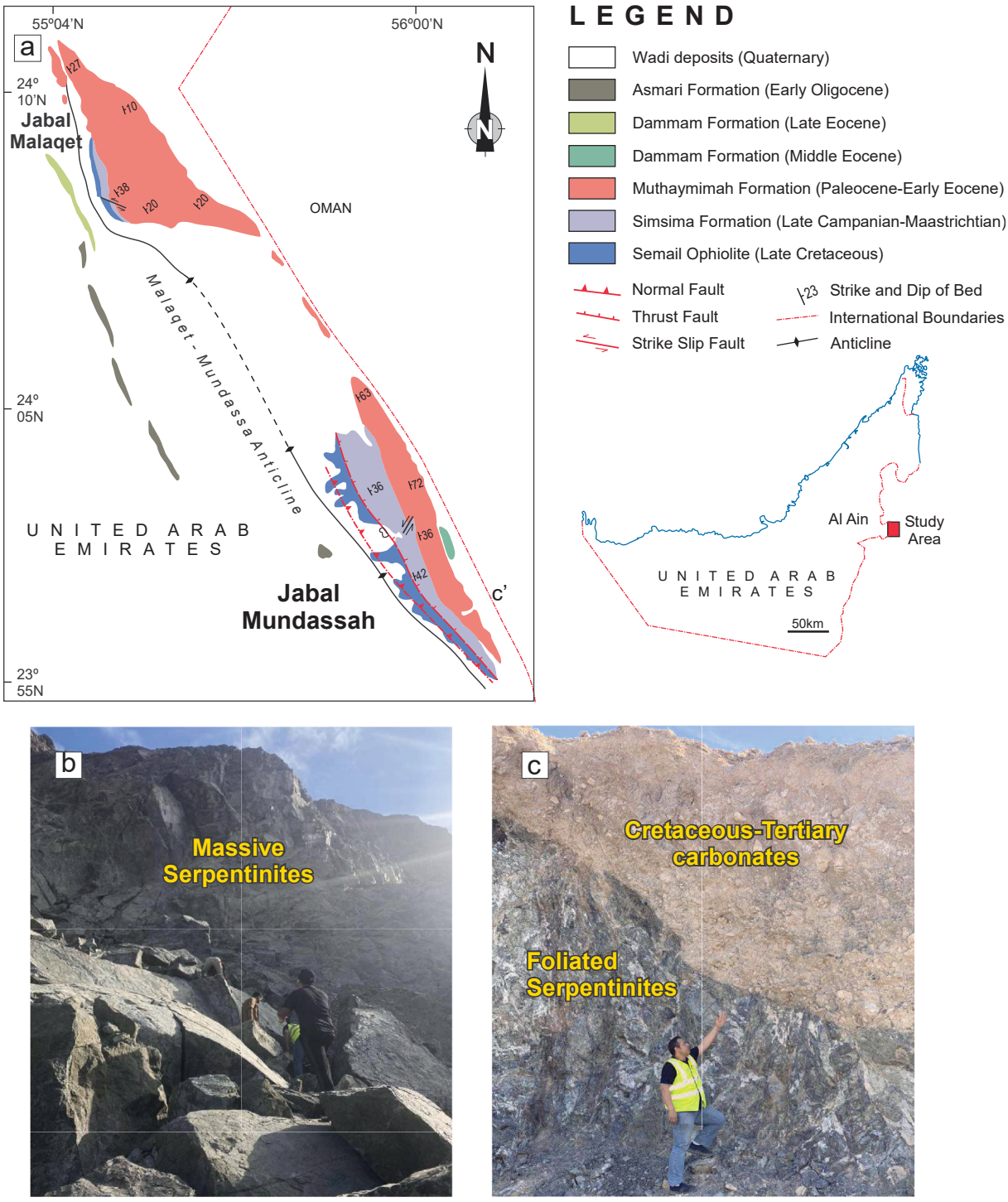

Fig. 2. (a) Simplified geologic map of Jabal Malaqet–Mundassah (JMM) area (modified from Abd El-Gawad et al., 2010; Faris et al., 2012), (b) Field image of massive serpentinites, (c) foliated serpentinites overlain by Cretaceous-Tertiary carbonates.

mantle source characteristics, tectonic evolution, and the broader dynamics of the Semail Ophiolite.

3. Analytical Methods

3.1. Electron microprobe mineral analyses

For mineralogical and petrographic analysis, polished thin sections were prepared and examined at the Department of Geosciences, UAE University. Some of the sections were carbon-coated for mineral analysis of serpentine and spinel. The microprobe analysis was conducted at the Department of Lithospheric Research, University of Vienna, Austria, using electron microprobe (CAMECA SX5) fitted with one Energy Dispersive X-ray Spectroscopy (EDS) and four Wavelength Dispersive X-ray Spectroscopy (WDS) spectrometers. During the analysis, acceleration voltage and beam current were set at 15kV and 20 nA, respectively, while the beam diameter was set to 5 μm. For the major element analysis, peak and background times of 20 and 10 seconds, respectively, were used, while for the trace element analysis, peak and background count times of 60 and 30 seconds, respectively, were applied. Both

synthetic and natural standards were used for calibration, and the Pouchou–Pichoir method (PAP) correction method was applied for the processing of raw data. Detection limits were typically ~0.02–0.05 wt.% for major oxides, with analytical uncertainties better than 2% relative.

3.2. X-ray diffraction analysis

The mineralogical composition of the bulk serpentinite samples was determined by X-ray diffraction (XRD) using a Rigaku SmartLab SE diffractometer at Wuhan Sample Solution Analytical Technology Co., Ltd. (Wuhan, China). The instrument was operated at 50 kV and 40 mA with Cu Kα radiation (λ = 1.54056 Å). Powdered samples were prepared by gentle grinding in an agate mortar and pestle and mounted as random specimens using the side-loading method to minimize preferred orientation. Diffraction data were collected over the range 3–70° 2θ, with a step size of 0.02° 2θ and a counting time of 1 s per step. Additional high-resolution low-angle scans (3–15° 2θ, step = 0.01°) were performed to identify possible antigorite superstructure reflections. The obtained diffraction patterns were processed to determine mineral phases and their relative proportions. The presence of superstructure reflections at low angles (<15° 2θ) and indexing to a long a-axis (≈ 40–50 Å) were taken as diagnostic of antigorite, whereas a simple stacking sequence without superstructure peaks (a ≈ 5.33 Å, c ≈ 7.27 Å) was used to identify lizardite.

3.3. Whole rock analysis

Analysis of major elements was conducted at the Central Analytical Facilities, Stellenbosch University using X-ray fluorescence (XRF) on fusion disks prepared with lithium tetraborate. To ensure homogeneity in the glass fusion disks used for XRF analysis, the samples were crushed and milled to a fine particle size of less than 70 μm. The loss on ignition (LOI) was calculated by measuring the weight difference of the samples after they were heated to a temperature of 1000°C. Analysis of trace elements and rare earth elements (REEs) was conducted at the Central Analytical Facilities Lab, Stellenbosch University, South Africa using Laser Ablation ICP-MS. An automated Claisse M4 Gas Fusion and ultrapure Claisse Flux equipment was used for the preparation of the fusion disks, employing a sample-to-flux ratio of 1:10. The samples were crushed and mounted onto a resin disk, where it was mapped and polished prior to the analysis of trace elements and REEs. A 193-nm Excimer laser from Applied Spectra, coupled with an Agilent 7700 Q ICP-MS, was used. Prior to the analysis, the ICP-MS was calibrated for optimal precision and minimal oxide ratios (< 0.2%) by adjusting both the laser and ICP settings while ablation was performed using NIST612 standard. Ablation was perfumed in helium gas, utilizing a 0.35-L/min flow rate, which was subsequently mixed with 0.9 L/min of argon and 0.003 L/min of nitrogen before entering the ICP plasma. For trace element analysis in fused samples, 104-μm spots were ablated at a frequency of 8 Hz and fluence of ~3.5 J/cm^2. Calibration was performed using the NIST 610 glass standard, with BHVO-2G and BCR-2G used as secondary standards to monitor accuracy and external reproducibility. Detection limits for most trace elements were <0.1 ppm, with external reproducibility better than 5% (1σ) based on repeated analyses of these reference materials. Fusion control standards (BHVO-1 and BCR-2) were run at the start of each analytical sequence to ensure consistent ablation of fused disks. The data was processed using the Norris Scientific LADR software (Norris and Danyushevsky, 2018).

For whole rock analysis of PGEs, a 30-gram sample is combined with a mixture of nickel oxide, sulfur, silica, borax, and soda ash, then heated to over 1000°C to create a nickel sulfide button. After weighing, the button was dissolved in hydrochloric acid after it was ground into a fine powder. Tellurides of the PGEs and gold are deposited onto a cellulose nitrate membrane filter, and subsequently dissolved in a mixture of nitric and hydrochloric acids. The resulting solution was analyzed at ALS Global using inductively coupled plasma–mass spectrometry (ICP-MS). Analytical precision was better than 1.0 wt.% for element compositions exceeding 5 wt.%. Detection limits for PGEs were generally 0.1–0.5 ppb, with reproducibility better than 10% (relative) at concentrations above 1 ppb, as verified by repeated analyses of international reference materials.

4. Results

4.1. Petrography and mineral chemistry

Photomicrographs and BSE images of JMM serpentinites reveal a dominant mineral assemblage of lizardite, antigorite, Cr-spinel, and altered olivine (Fig. 3a–f). The serpentine species were identified using petrographic criteria and backscattered electron (BSE) imaging. Lizardite exhibits a distinct fibrous texture with parallel alignment of fibers, creating a linear, banded appearance characteristic of foliated serpentinites (Fig. 3a, b). Antigorite contrasts with lizardite by its massive to granular texture and its occurrence as interstitial fillings between lizardite fibers. Petrographic and BSE observations reveal mesh-, vein-, and ribbon-textured serpentine consistent with serpentinization of an olivine-rich protolith, while electron-microprobe analyses define Si–Mg trends typical of lizardite–antigorite solid solution. Because these petrographic and compositional features alone cannot discriminate serpentine polymorphs, X-ray diffraction (XRD) was used for definitive phase identification (ESM 1). The XRD patterns display a dominant basal reflection at ~12° 2θ (d ≈ 7.2–7.3 Å), with Serp-1 characterized by a lizardite-1T pattern and Serp-2 showing additional low-angle reflections indicative of antigorite. These crystallographic data confirm the presence and co-occurrence of lizardite and antigorite in the JMM serpentinites, consistent with the observed microtextures and mineral chemistry.

Chromite spinel occurs as opaque black grains within the serpentine matrix (Fig. 3b). Altered olivine exhibits a distinctive granoblastic texture with fibrous serpentine aggregates along irregular, curved boundaries, indicating the replacement of olivine by serpentine during serpentinization (Fig. 3c). The BSE image (Fig. 3d) shows Cr-spinel grains enclosed in a fine-grained matrix of antigorite and lizardite. The Cr-spinels exhibit irregular margins, indicating partial alteration during serpentinization of the ultramafic protolith. In other BSE views, antigorite generally appears darker than lizardite, although local variations in gray tone (Fig. 3e) reflect compositional or orientation differences between grains. Cr-spinel grains are large, elongated, and highly fractured, and are often rimmed by altered sulfides (Fig. 3f).

Serpentine-group minerals (antigorite and lizardite) and accessory Cr-spinel were analyzed to constrain the mineralogical evolution and geochemical fingerprint of the studied serpentinites. Representative ranges of major oxides (wt.%) and calculated cations (apfu) are summarized in ESM2 Table 1. Antigorite displays SiO_2 contents ranging from 36.85–41.72 wt.%, Al_2O_3 from 1.66–2.93 wt.%, and FeO from 4.99–7.82 wt.%, with minor Cr_2O_3 (up to 1.01 wt.%). MgO contents are relatively high (35.20–36.77 wt.%), consistent with its Mg-rich composition. The corresponding cationic proportions (apfu) vary between Si = 1.75–1.91, Al = 0.09–0.16, Fe^t = 0.19–0.31, and Mg = 2.45–2.59 (Mg# = 89.32–91.47).

Lizardite shows broadly similar compositions, with SiO_2 ranging from 36.68–42.08 wt.%, Al_2O_3 from 0.02–0.88 wt.%, and FeO from 3.52–11.27 wt.%. MgO contents are higher and more variable (30.73–39.36 wt.%) compared to antigorite. In terms of apfu, lizardite has Si = 1.79–1.92, Al = 0.00–0.05, Fe^t = 0.13–0.47, and Mg = 2.30–2.69 (Mg# = 89.32–9.472). Compared to antigorite, lizardite is typically more Fe-rich and Al-poor. On the SiO_2–MgO diagram (Fig. 4a), the majority of both lizardite and antigorite analyses plot within the "antigorite with interpenetrating texture" field. A smaller subset of lizardite compositions occurs within the "lizardite after metamorphic olivine (pseudomorphic)" field, while a few antigorite data points fall between these two domains. This indicates that the bulk of the

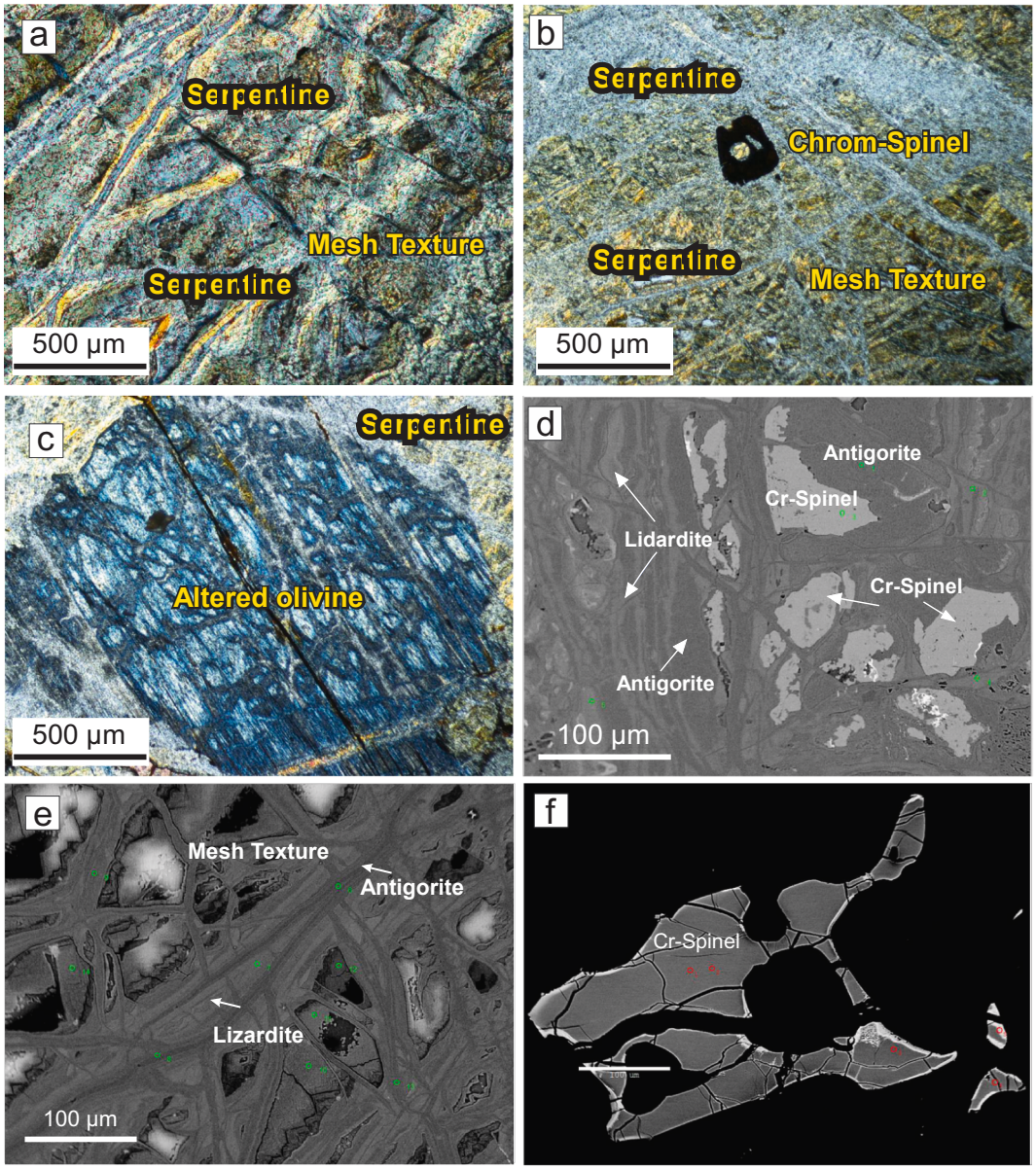

Fig. 3. (a–c). Photomicrographs of serpentinites viewed under crossed polarized light (XPL), **(d–f)** Backscattered Electron Images (BSE) images serpentinites from the JMM serpentinites.

serpentine minerals, regardless of petrographic identification, share overlapping MgO–SiO_2 compositions comparable to those of antigorite with interpenetrating textures.

The chemical compositions of Cr-spinel from the analyzed serpentinites are presented in ESM2 Table 2. The Cr-spinel samples exhibit a range of chemical compositions, with SiO_2 (0.02–0.07 wt.%) and TiO_2 (0.02–0.03 wt.%) showing very low concentrations. Al_2O_3 (29.24–31.38 wt.%) and Cr_2O_3 (34.51–38.39 wt.%) are notably high. FeO (16.23–18.78 wt.%) and MgO (13.47–14.06 wt.%) are moderately high, while MnO (0.63–0.70 wt.%) and NiO (0.11–0.15 wt.%) are present in low amounts. The Cr-spinels exhibits low Cr# [Cr/(Cr+Al) < 0.5; 0.42–0.48] and high Mg# [Mg/(Mg+Fe^{2+}) > 0.5; 0.58–0.61], consistent with typical spinel compositions (Fig. 4b; Kapsiotis et al., 2009). Cr-spinels from the Oman ophiolite, characterized by high Cr# (>0.5), plot mainly within the chromite and magnesiochromite fields, with only a few extending into the spinel field (Fig. 4b). In the MnO versus Cr# discrimination diagram (Fig. 4c), some Cr-spinel analyses show MnO contents approaching the upper limit of the primary Cr-spinel field. The analyzed grains are texturally homogeneous, lack ferritchromite rims, and display high Mg# (0.58–0.61) and moderate Cr# (0.42–0.48), indicating preservation of primary magmatic compositions. Minor Mn enrichment is therefore interpreted as reflecting primary crystallization under relatively oxidizing mantle conditions and/or limited subsolidus re-equilibration during serpentinization, rather than formation of secondary Cr-spinel. The apfu values of the Cr-spinel yield Cr = 6.69–7.94, Al = 8.26–9.29, Fe^{2+} = 0.13–3.97, and Mg = 0.03–4.99, showing wide variability in Fe^{2+}–Mg substitution. All analyzed spinels plot in the ophiolitic complex field (Fig. 4d).

The ternary Cr-Al-Fe^{3+} classification diagram (Fig. 4e) shows that the JMM spinels fall largely within the Cr-spinel field commonly associated with fore-arc peridotites. However, their compositions also partly overlap with spinels from abyssal serpentinites (Fig. 4f).

4.2. *Bulk rock geochemistry*

The whole-rock major element compositions of the JMM serpentinites, normalized to an anhydrous volatile-free basis, are presented in ESM2 Table 3. They are characterized by high MgO (34.94–39.15 wt.%)

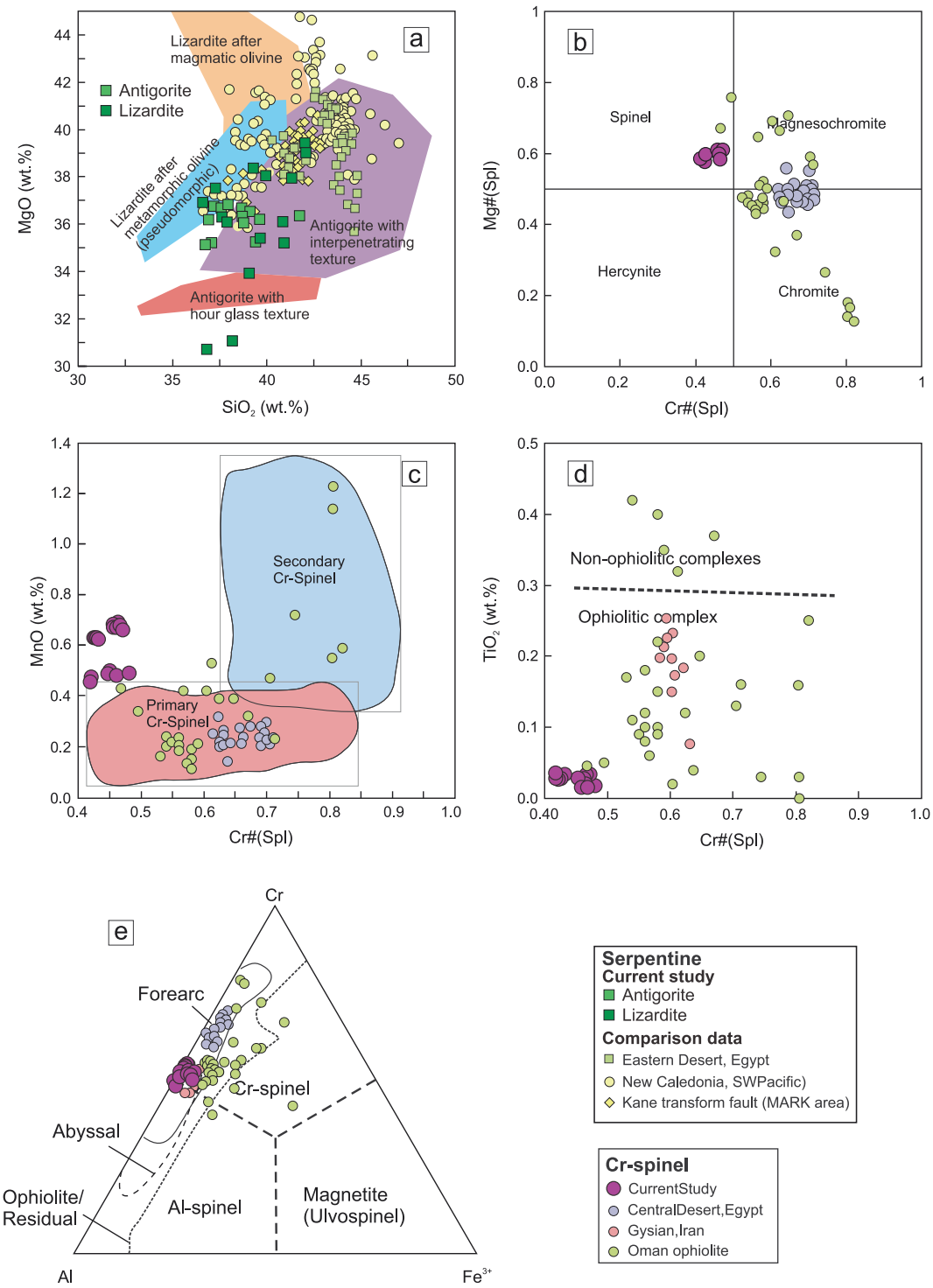

Fig. 4. Microprobe analyses of serpentinites are plotted in (a) SiO_2 vs. MgO (after Wicks, 1979), Serpentinite comparison data for the Central Eastern Desert, Egypt, are from Ali et al. (2021) and Abdelfadil et al. (2024); ophiolitic serpentinites comparison data from New Caledonia, SW Pacific (after Ulrich et al., 2020) and Kane transform fault, MARK area (after Andréani et al., 2007). Microprobe analyses of Cr-spinel are plotted in (b) Cr# (Cr/Cr + Al) vs. Mg# (Mg/Mg + Fe^{2+}) diagram; (c) Cr# (Cr/Cr + Al) vs. MnO diagram. Fields of primary and secondary chromian spinel are after Khedr, et al. (2017); (d) Cr# vs. TiO_2 diagram and (e) Al-Cr-Fe^{3+} ternary diagram (after Barnes & Roeder, 2001). Fields of ophiolitic and non-ophiolitic complexes are after Modjarrad et al. (2024). Comparison data of Cr-spinel from Oman Ophiolite (after Arai et al., 2020 & Ahmed and Arai, 2002), Centra Eastern Desert, Egypt (after Abdelfadil et al., 2024); from Gysian ophiolitic serpentinites, Iraq (after Modjarrad et al., 2024).

and low Al_2O_3 (0.21–0.92 wt.%), TiO_2 (0.01–0.03 wt.%), and alkali contents (Na_2O+K_2O = 0.02–0.04 wt.%). Compared with the global serpentinite database of Deschamps et al. (2013), these values overlap with the lower ranges of abyssal serpentinites (MgO = 26.6–43.4 wt.%; Al_2O_3 = 0.04–6.39 wt.%; TiO_2 = 0.004–0.06 wt.%; Na_2O+K_2O = 0.01–0.46 wt.%) but are more consistent with subduction-zone serpentinites, which are similarly depleted in Al_2O_3 and TiO_2 (0.02–20.7 wt.% and 0.01–1.34 wt.%, respectively). Mantle wedge serpentinites show broader compositional ranges that encompass the JMM values, but the systematic depletion in Al and Ti in JMM samples is a diagnostic feature

commonly associated with forearc and subduction-related settings. High loss on ignition values (13.02–15.97 wt.%) confirm significant hydration during serpentinization, consistent with the petrographic observation of scarce relict pyroxene. Despite serpentinization, bulk-rock compositions retain meaningful protolith geochemical signatures (Deschamps et al., 2013).

The JMM serpentinites contain elevated concentrations of compatible elements (Ni = 686–2462 ppm, Cr = 337–3143 ppm, Co = 57.3–118 ppm, V = 12.4–70 ppm). These values plot well within the fields of subduction-zone serpentinites (Ni = 111–7427 ppm; Cr = 201–6302 ppm; Co = 53–151 ppm; V = 8–241 ppm) and partly overlap with abyssal serpentinites (Ni = 36–3760 ppm; Cr = 37–10,033 ppm; Co = 9.3–219 ppm; V = 1–200 ppm). However, the consistently high Ni and Cr coupled with low V contents of the JMM samples suggest derivation from highly depleted harzburgitic protoliths, a hallmark of subduction forearc serpentinites rather than abyssal types, which often show greater compositional heterogeneity.

Incompatible trace elements are also distinctive. The JMM serpentinites are enriched in LILE (Rb = 0.29–3.86 ppm; Sr = 7.8–68.7 ppm; Ba = 0.85–39.5 ppm; K = 70–288 ppm), within the narrow but enriched ranges of subduction-zone serpentinites (Rb = 0.02–9.5 ppm; Sr = 0.25–733 ppm; Ba = 0.044–143 ppm; K = 25–4732 ppm). By contrast, abyssal serpentinites typically show lower and more variable Ba and Sr contents, reflecting the lack of fluid addition. This LILE enrichment is interpreted as the imprint of slab-derived fluids and is diagnostic of subduction settings (Deschamps et al., 2013).

JMM serpentinites also exhibit moderate enrichments in Ti (50.6–151 ppm) and P (21.8–43.6 ppm) and are strongly depleted in Th (0.01–0.03 ppm), U (0.03–0.10 ppm), and Pb (0.89–6.30 ppm). These values are consistent with the restricted ranges of subduction-zone serpentinites, which tend to have low Th–U contents relative to abyssal counterparts. The high-field strength elements (Nb = 0.03–0.07 ppm; Zr = 0.05–0.48 ppm; Hf = 0.006–0.031 ppm; Ta = 0.002–0.006 ppm) are uniformly depleted and lie at the lower limits of global serpentinite fields.

The rock/primitive mantle pattern of the JMM serpentinites (Fig. 5a) are comparable to the typical subduction zone serpentinites (Deschamps et al., 2013). They are characterized by strong enrichment in fluid-mobile elements (Ba, U, Sr, Pb) and depletion in HFSE (Nb, Ta, Ti, Zr), are typical of forearc serpentinites formed through fluid–rock interaction in subduction channels. The samples exhibit low rare earth element (REE) contents. Chondrite-normalized REE patterns of the JMM serpentinites exhibit somewhat U-shaped trends, characterized by variable enrichment in light rare earth elements (LREE; La–Sm) and heavy rare earth elements (HREE; Gd–Lu), together with depletion in middle rare earth elements (MREE; Eu–Dy). These features are comparable to published subducted serpentinites derived from harzburgitic protoliths (Fig. 5b). The chondrite-normalized REE patterns also show a variable range of HREE enrichment (Gd/Yb_N = 0.15–0.82; Dy/Yb_N = 0.076–0.782) relative to the LREE (La/Sm_N = 0.15–2.55; La/Yb_N = 0.10–2.06) (Fig. 5b). While some samples exhibit HREE enrichment (Gd/Yb_N and $Dy/Yb_N < 1$), others display LREE enrichment (La/Sm_N and $La/Yb_N > 1$).

The PGEs concentrations in the analyzed serpentinite samples are detailed in ESM2 Table 4. The PGEs reveal a range of values, with Ir (1.45–4.65 ppb), Os (1.25–4.13 ppb), Pd (2.33–6.08 ppb), Pt (2.18–6.85 ppb), Rh (0.45–1.51 ppb), and Ru (0.86–2.35 ppb) showing moderate to high contents. Higher values are observed for Pt (2.18–6.85 ppb) and Pd (2.33–6.08 ppb), while Rh (0.45–1.51 ppb) and Ru (0.86–2.35 ppb) exhibit lower concentrations. On average, Pt and Pd (means = 4.42 ± 1.87 and 3.95 ± 1.51 ppb, respectively) are notably higher than Os–Ir–Ru (means = 2.84 ± 1.21, 3.05 ± 1.15, and 1.51 ± 0.64 ppb, respectively), with relative standard deviations between 20 and 35%, indicating moderate compositional variability.

5. Discussion

5.1. Robust geochemical proxies and mantle protolith

Interpretation of the tectonic setting and mantle protolith of the JMM serpentinites requires first identifying which geochemical signatures preserve primary igneous information and which have been modified by serpentinization and associated fluid–rock interaction (Deschamps et al., 2013). The HFSE (e.g., Ti, Nb, Zr, Hf, Y), Al, Cr, Mg# and PGEs, particularly the Ir-group PGEs (IPGE: Os, Ir, Ru), are considered largely immobile during low-temperature serpentinization and hydrothermal alteration (e.g., Pearce et al., 2000; Deschamps et al., 2013; Paulick et al., 2006). Primary cores of Cr-spinel reliably record protolith melting and tectonic affinity (Dick & Bullen, 1984; Arai, 1994), and empirical calibrations of Cr# allow first-order estimates of melt fraction (Kamenetsky et al., 2001). Spinel core compositions are typically resistant to low-T alteration (Bach et al., 2006), although metasomatic modification of rims/host peridotites can occur (Gamal El Dien et al., 2019) and cores must therefore be identified texturally. In contrast, large-ion lithophile elements (LILE: e.g., Ba, Sr, Pb, Cs, Rb), boron, sulfur, and to some extent the Pd-group PGEs (PPGE: Pt, Pd, Rh) are fluid-mobile and can be enriched or redistributed during serpentinization and metasomatism (e.g., Scambelluri et al., 2019; Barrett et al., 2022). Rare earth elements (REEs) may be affected by fluid-mediated processes, but their overall patterns and HFSE ratios often preserve magmatic trends (Schmidt et al., 2009; Ague, 2017). With this framework, we interpret the primary history of the JMM mantle section,

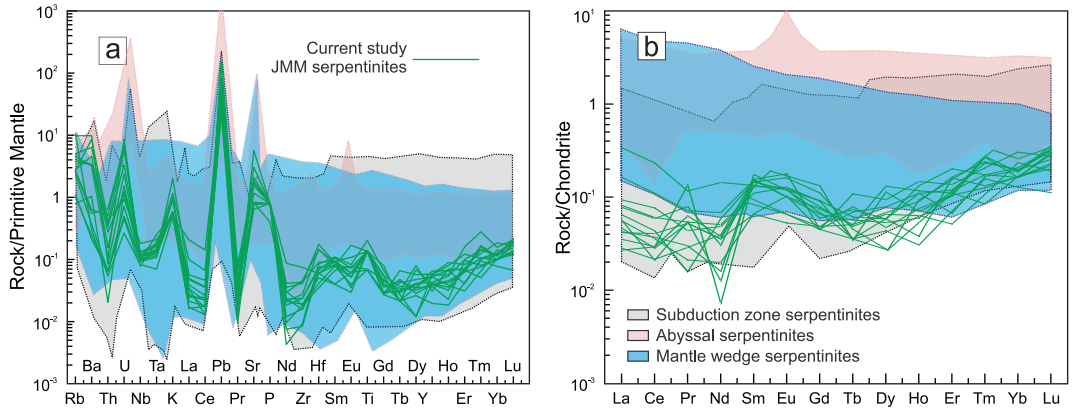

Fig. 5. (a) Primitive mantle-normalized trace element patterns, (b) Chondrite-normalized REE patterns of JMM serpentinites. Normalization values are from McDonough and Sun (1995). Comparison data of subducted, mantle wedge, and abyssal serpentinites derived from harzburgite are obtained from Deschamps et al. (2013).

recognizing where secondary overprints provide additional petrogenetic context.

Given the extensive serpentinization of the JMM serpentinites, the modal-based ultramafic classification of Streckeisen (1976) is unsuitable because alteration obscures the original proportions of olivine, clinopyroxene, and orthopyroxene. Although relic bastite textures locally record former pyroxenes (Viti & Mellini, 1998), their sparse preservation prevents reliable modal estimation (Mével, 2003). Consequently, whole-rock geochemistry is used to infer the protolith. The serpentinites display high Mg# (89.32–91.47), SiO_2 (35.87–40.90 wt.%), and extremely low La_N (0.009–0.12) values (ESM2 Table 3), plotting mainly within the dunite field with minor excursions into the harzburgite field (Fig. 6a, b; Le Maitre, 2002). These geochemical signatures, together with elevated Ni (≤2462 ppm), Cr (≤3143 ppm), and Co (≤118 ppm) (ESM2 Table 3) and low CaO and Al_2O_3 contents (Fig. 6c), are consistent with residues of extensive melt extraction from highly depleted mantle peridotites (Deschamps et al., 2013), indicating refractory dunite–harzburgite protoliths. The tectonic setting of this melting event is constrained by robust, immobile element ratios. The low Al_2O_3/SiO_2 (< 0.03) and MgO/SiO_2 (< 1.1) ratios overlap precisely with the field for global forearc serpentinites (Fig. 6d; Pearce et al., 2000). The extremely low TiO_2 contents (0.008–0.025 wt.%, Fig. 6e) are a key indicator, as Ti behaves as a relatively immobile element during low-temperature serpentinization compared with LILE, and shows no systematic covariance

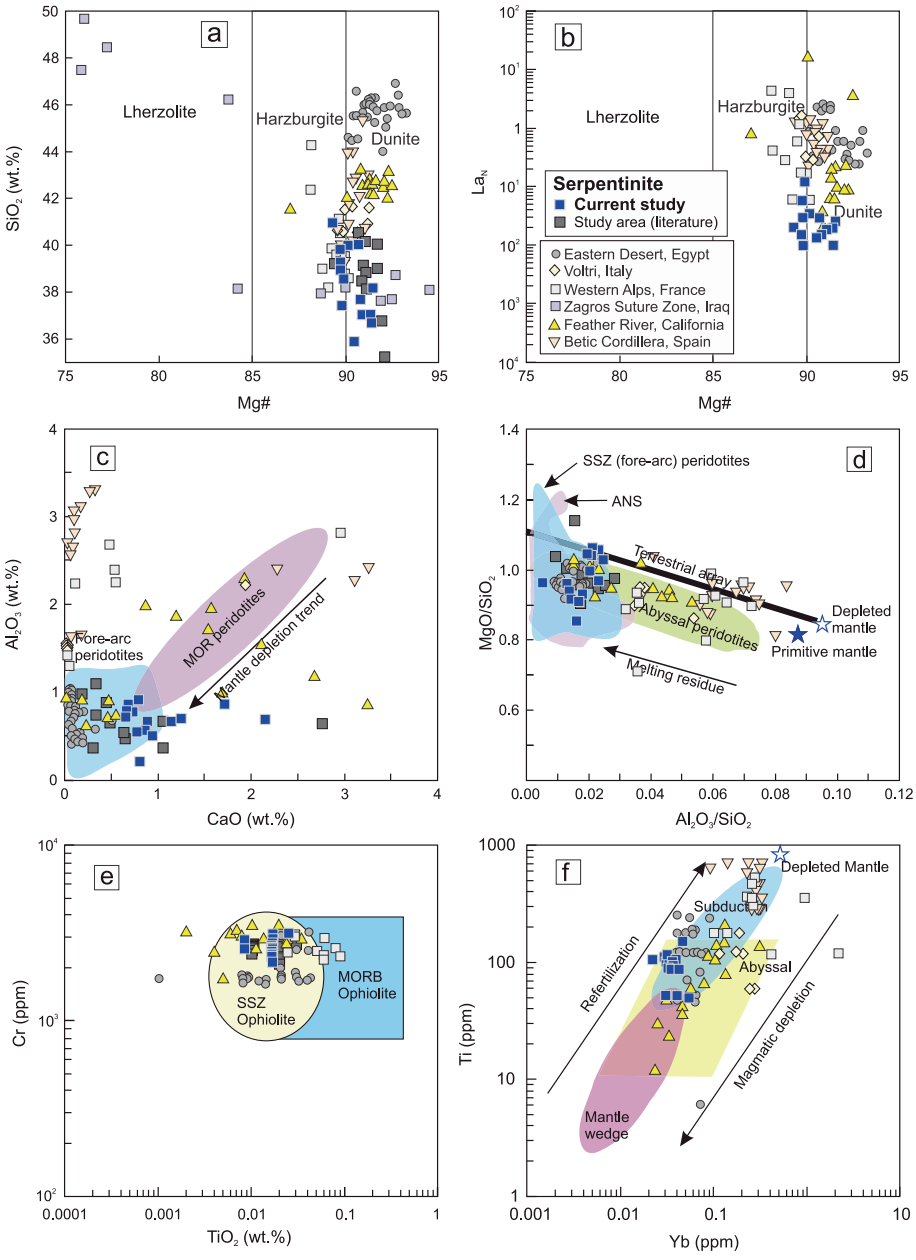

Fig. 6. Plots of whole rock Mg# vs. (a) SiO_2 and (b) La_N, indicating a dunite-harzburgite protolith. Discrimination fields for Mg#, SiO_2 and La_N are based on Le Maitre (2002). Chondrite normalization values were sourced from McDonough and Sun (1995); (c) CaO vs. Al_2O_3 diagram (after, Ishii et al., 1992); (d) Al_2O_3/SiO_2 vs. MgO/SiO_2 diagram; (e) TiO_2 vs. Cr diagram (after Pearce et al., 1984); (f) Yb vs. Ti diagram (after Deschamps et al., 2013). The "terrestrial array" represents the bulk silicate Earth evolution (Hart and Zindler, 1986). Fields of abyssal and fore-arc peridotite are after Niu (2004); Pearce et al. (2000) and Parkinson and Pearce (1998). ANS ophiolitic peridotite field is after (Ahmed and Habtoor, 2015). Serpentinite comparison data for the Eastern Desert, Egypt, are from Ali et al. (2021) and Abdelfadil et al. (2024); Voltri Massif, Italy (after Cannaò et al., 2016); Western Alps, France (after Chalot-Prat et al., 2003); Zagros suture zone, Iraq (after Monsef et al., 2018), Feather River region, California (after Li and Lee, 2006); and Betic Cordillera, southern Spain (Garrido et al., 2005).

with LOI or LILE in the JMM dataset, supporting preservation of a primary protolith signal (Modjarrad et al., 2025). This pronounced Ti depletion, alongside low Yb and high Cr (Fig. 6e, f), signifies melt extraction within a supra-subduction zone (SSZ) mantle wedge, a setting characterized by highly refractory peridotites (Parkinson & Pearce, 1998). While a few samples plot near abyssal peridotite fields (Fig. 6c, f), the collective evidence from HFSE depletion and diagnostic Cr-spinel and PGE systematics (discussed below) firmly supports a fore-arc SSZ origin (Deschamps et al., 2013). These few abyssal-like data points likely reflect localized sampling of less-depleted mantle domains or small-scale chemical heterogeneity within the fore-arc mantle wedge, rather than a fundamentally abyssal protolith for the JMM suite.

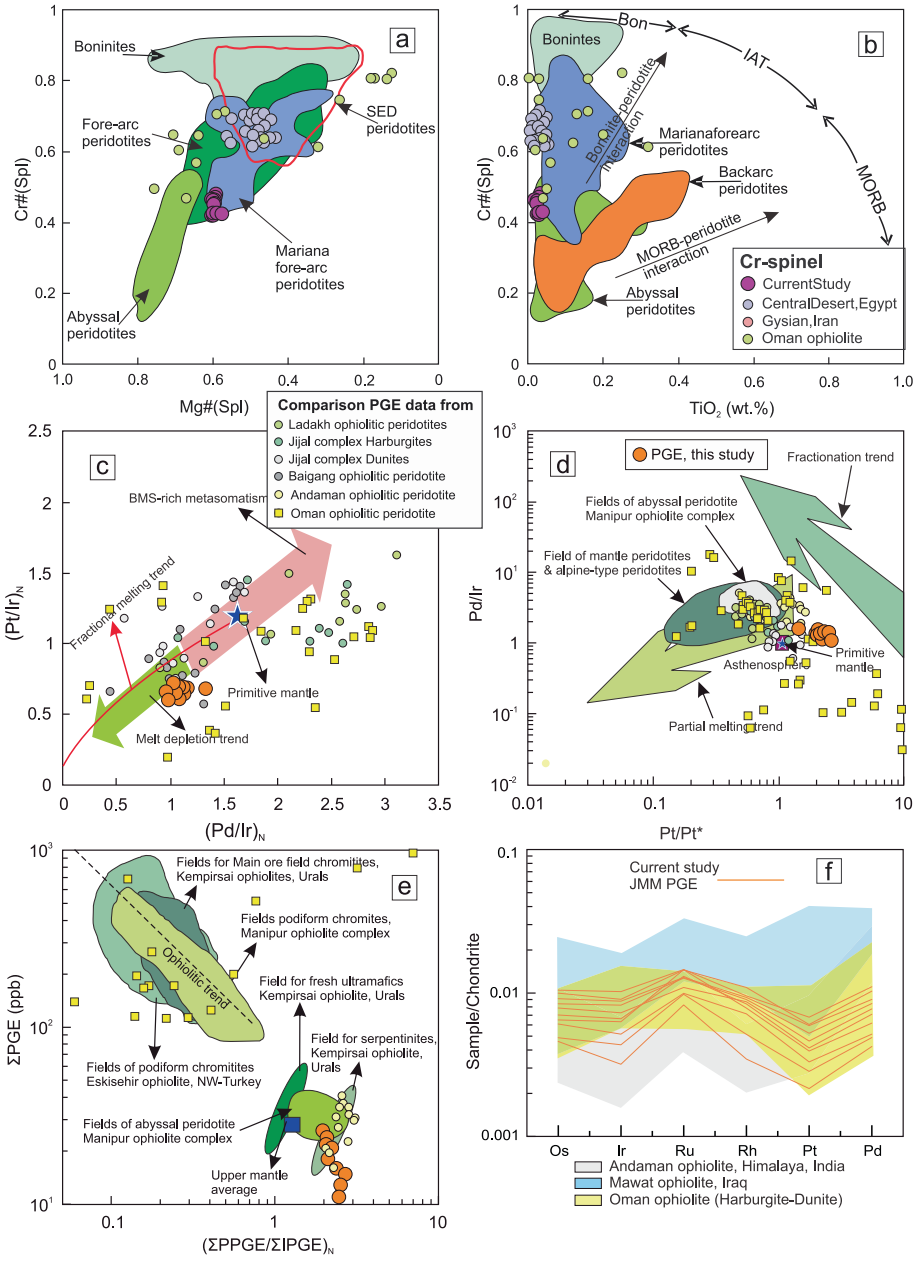

Fig. 7. Microprobe analyzes of JMM Cr-spinel plotted in (a) Mg# vs. Cr# variation diagram (after Pearce et al., 2000), showing that the JMM spinels plot within the forearc peridotite field and overlap with Mariana forearc peridotite compositions; (b) TiO_2 vs. Cr# variation diagrams (after Pearce et al., 2000) where the JMM spinels plot mainly within the abyssal peridotite field, with minor overlap toward the boninite–peridotite interaction field. Fields of chromian spinel in forearc peridotites (after Dick & Bullen, 1984), boninites (Barnes & Roeder, 2001), abyssal peridotites (after Dick & Bullen, 1984), Mariana forearc peridotites (Ohara & Ishii, 1998), SED peridotites (Farahat et al., 2011). Cr-spinel comparison data from Oman Ophiolite (after Arai et al., 2020 & Ahmed and Arai, 2002), Central Eastern Desert, Egypt (after Abdelfadil et al., 2024); Gysian ophiolitic serpentinites, Iraq (after Modjarrad et al., 2024). Plots of whole rock PGEs compositions of JMM serpentinites.(c) $(Pt/Ir)_N$ vs. $(Pd/Ir)_N$. For comparison are displayed Baigang peridotites, Tibet (after Xu et al. 2020) western Ladakh peridotites (after Bhat et al. 2021), and Jijal harzburgite and dunites (after Zafar et al., 2024); fractional and metasomatic trends from Bhat et al. (2021). (d) Pt/Pt* vs. Pd/Ir. Fractionation and partial melting trends are from Garuti et al. (1997). Fields for mantle peridotite and alpine type peridotite (Garuti et al., 1997) and peridotites from Manipur ophiolite belt (Singh, 2013) are also shown. (e) chondrite-normalized ΣPPGE/ΣIPGE vs. ΣPGE plot. Upper mantle values and ophiolitic trend are from Melcher et al. (1999) respectively. For comparison, fields for podiform chromitites and peridotites from the Manipur Ophiolite Complex (Singh, 2013); main ore field chromitites, Kempirsai ophiolite massif, Urals (Melcher et al., 1999), podiform chromitites, Eskisehir ophiolite NW-Turkey (Uysal et al., 2009) are shown. (f) Chondrite normalized PGEs patterns. Normalizing factors are from McDonough and Sun (1995). The fields of Andaman ophiolite, Himalaya, India from Saha et al. (2018), Mawat ophiolite, Iraq from Ismail et al. (2010), and Oman ophiolite from Ahmed (2024) and Hanghøj et al. (201). All peridotites are subduction-zoned type.

5.2. Tectonic setting and comparison with the Semail Ophiolite

The nearby Semail ophiolite, a classic example of obducted Neo-Tethyan oceanic lithosphere, provides a critical regional analogue. Its formation is interpreted as the product of intra-oceanic subduction initiation and subsequent seafloor spreading in a supra-subduction zone setting, culminating in its Late Cretaceous obduction onto the Arabian margin (e.g., Searle & Cox, 1999; Rioux et al., 2016). The mantle section of the Semail ophiolite is predominantly composed of highly depleted harzburgites with dunite channels, reflecting high degrees of partial melting.

A detailed comparison reveals both similarities and important distinctions. The JMM Cr-spinels have Cr# (0.42–0.48) and Mg# (0.58–0.61) that are consistent with formation from a highly depleted mantle residue, yet their Cr# is notably lower than many Semail spinels, which commonly exhibit Cr# from 0.43 to >0.8 (Ahmed & Arai, 2002; Arai et al., 2020; Cocomazzi et al., 2020) (ESM3 Table 1, Fig. 7a, b). This indicates a marginally lower, but still high, degree of melt extraction for the JMM protolith. This contextualization is further refined by considering the heterogeneous nature of the Semail mantle as revealed by detailed studies of its basal sections. Prigent et al. (2018) documented that the basal "banded unit" peridotites directly overlying the metamorphic sole show evidence of significant syn-deformational metasomatic refertilization by slab-derived hydrous fluids during the earliest stages of subduction. This process generated localized domains of more fertile lithologies (Cpx-rich harzburgites to lherzolites) and is characterized by extreme enrichment in fluid-mobile elements (e.g., B, Li, Cs) and crystallization of amphibole, signatures indicative of intense, channelized fluid flux in a nascent mantle wedge shear zone. Indeed, the JMM serpentinites record LILE enrichment consistent with slab-derived fluids (Zhang et al., 2021). However, these values are moderate compared with the extreme enrichments reported for intensely metasomatized Semail basal shear zones (Prigent et al., 2018). Moreover, neither petrography nor XRD shows amphibole crystallization, indicating a regional slab-fluid overprint (Evans, 2004) rather than extreme, amphibole-bearing basal-shear metasomatism. This key distinction suggests that the JMM fragment was not subjected to the intense, focused fluid–rock interaction that affected the basal Semail shear zone. Instead, the JMM likely represents a slice of the more typical, highly depleted fore-arc mantle wedge situated above this localized metasomatic front. This is consistent with fore-arc mantle analogues from the Izu–Bonin–Mariana and Tonga systems where extreme metasomatism is similarly restricted to narrow shear zones or channels (Parkinson & Pearce, 1998). Moreover, while Prigent et al. (2018) demonstrate that fertile compositions occur in specific tectonic settings within Oman, the JMM geochemistry aligns more closely with the depleted end of the mantle spectrum, supporting its interpretation as a less-modified fragment of fore-arc lithosphere tectonically juxtaposed against more complexly metasomatized Semail sequences.

The PGE systematics underscore this difference. The JMM serpentinites show low total PGE abundances (ΣPGE ≈ 15–35 ppb; calculated as the sum of Os, Ir, Ru, Rh, Pt and Pd; ESM2 Table 4), which are consistent with sulfide exhaustion during high-degree melting (Maier et al., 2003; Zaccarini et al., 2022), although locally higher ΣPGE may occur in chromitite- or sulfide-rich microdomains in other SSZ settings (González-Jiméne et al., 2014). Their near-chondritic IPGE/PPGE ratios are characteristic of such residues. The JMM PGEs plot along the primitive mantle melt depletion trend (Fig. 7c), and their specific ratios are diagnostic. The low Pd/Ir ratios (1.18–1.61) and elevated Pt/Pt* ratios (1.43–2.43) align with the partial melting array and are distinct from the compositional field of highly fluid-fluxed mantle wedges (Fig. 7d). However, they are not as extremely depleted as some Oman peridotites, which can have ΣPGE contents exceeding 1000 ppb in chromitites (Fig. 7e) and show more pronounced IPGE enrichment (Ahmed, 2024; Hanghøj et al., 2010). This is further evident in the chondrite-normalized patterns (Fig. 7f), where the JMM suite shows stronger Ir depletion and more balanced Pd-Pt anomalies compared to the Oman patterns, which have higher absolute PGE levels and less pronounced Ir depletion. This contrast suggests that while both mantle sections experienced high-degree melting in an SSZ setting, the JMM fragment represents a domain that underwent slightly less extreme melting and, crucially, was not subjected to the same degree of late-stage metasomatic sulfide addition or chromite-controlled PGE segregation that affected parts of the Oman mantle. This supports the interpretation that the JMM captures an earlier or less mature stage of fore-arc development.

Therefore, we interpret the JMM serpentinites not as a fragment of the main Semail oceanic crust, but as a highly depleted fore-arc mantle slice that was tectonically juxtaposed against it during obduction. It represents a fragment of the depleted fore-arc mantle wedge that was not subjected to the intense, late-stage metasomatism or extreme melt-rock interaction documented in specific Semail shear zones. It likely represents an older or laterally distinct fragment of the Neo-Tethyan fore-arc lithosphere, capturing a stage of mantle depletion that was extensive but preserved a less modified magmatic and metasomatic history.

5.3. Redox conditions and secondary modification

Although pervasive serpentinization precludes direct thermobarometry, qualitative redox constraints for the JMM serpentinites are inferred from V–MgO systematics (Fig. 8a; Lee et al., 2003), following calibrations that demonstrate V partitioning is strongly dependent on oxygen fugacity (fO_2) (Canil, 2002; Mallmann & O'Neill, 2009). The use of V is justified because stable isotope and whole-rock studies confirm it is not systematically remobilized during serpentinization, thereby preserving a primary igneous redox signature where hydrothermal leaching is limited (Prytulak et al., 2013). The JMM data plot along a trend suggestive of relatively elevated fO_2 conditions (around FMQ+2) (Fig. 8a), but this estimate remains qualitative because MgO is reported on a hydrous basis and no rehydration correction was applied. Notably, the measured MgO contents are on a hydrous basis and are lower than the anhydrous values used in the model trends (Lee et al., 2003); thus, the diagram provides a qualitative redox indicator rather than a precise fO_2 calculation. This interpretation of relatively oxidized conditions is corroborated by the petrographic ubiquity of magnetite. The elevated fO_2 is consistent with modification by slab-derived, oxidizing fluids in a fore-arc environment. Complementary petrographic observations, particularly the presence of magnetite along serpentine veins and the coexistence of antigorite with lizardite, provide mineralogical evidence for oxidation during fluid–rock interaction at elevated fore-arc temperatures (Hilairet et al., 2006; Beard et al., 2009).

The bulk-rock geochemistry reveals the distinct geochemical imprint of this fluid overprint on the protolith. Primitive mantle-normalized patterns show the diagnostic SSZ decoupling: strong depletion in immobile HFSE (Nb, Ta, Ti, Zr) contrasting with marked enrichment in fluid-mobile LILE (e.g., Ba, Sr, Pb) (Fig. 5a). This is the definitive fingerprint of interaction with slab-derived fluids (Pearce, 1982; Pearce & Stern, 2006). Chondrite-normalized REE patterns are generally flat to weakly U-shaped (Fig. 5b), with variable LREE enrichments in some samples attributable to limited and heterogeneous metasomatism by these fluids (Deschamps et al., 2013).

The JMM serpentinites exhibit LREE-enriched patterns with $(La/Sm)_N = 0.15–2.55$, plotting between modeled residual harzburgites and crustal-/MORB-contaminated peridotites (Fig. 8b; Sharma & Wasserburg, 1996). Their elevated Zr/Hf (4.0–45.5) and Nb/Ta (6.6–20.8) ratios indicate slab-derived melt/sediment refertilization, while negative Zr anomalies (Fig. 5a) denote limited crustal input (Taylor & McLennan, 1985), pointing to multi-source SSZ-type metasomatism. The significant LREE-HFSE decoupling highlights a dominant fluid-rock (hydrothermal) overprint, akin to serpentinites from Egypt, California, and France but distinct from the Spanish Betic Cordillera (Fig. 8c). This

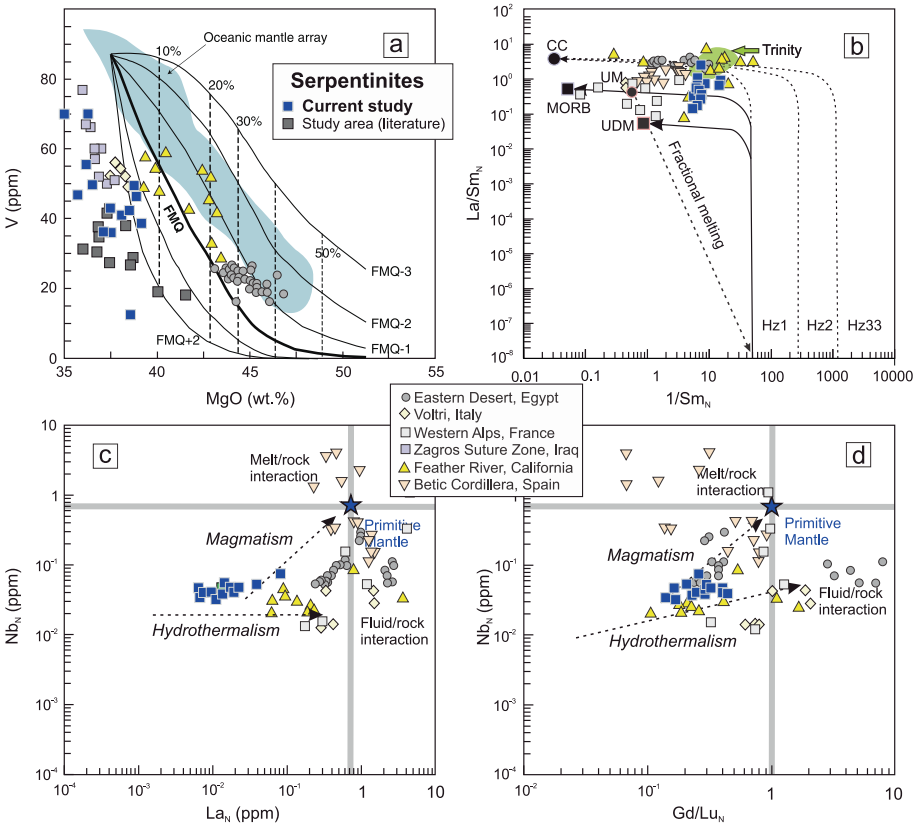

Fig. 8. (a) Plot of whole rock V vs. MgO diagram (recalculated under anhydrous forms) illustrating melting degrees and oxygen fugacities modeling (after Lee et al., 2003). Curves represent partial melting trend at 1 log unit intervals, spanning fO_2 from FMQ−3 to FMQ+2 (thick solid curve is for FMQ). Dashed lines represent the degree of melt extracted in 10% increment (Lee et al., 2003); (b) Chondrite-normalized $(1/Sm)_N$ vs. $(La/Sm)_N$ diagram (after Sharma and Wasserburg, 1996). MORB mid-ocean ridge basalts, UM upper mantle composition, UDM ultra-depleted melt composition, CC continental crust composition, HZ1, HZ2 and HZ3 model dunite-harzburgite compositions. Fields of Trinity ophiolite is shown for comparison (Gruau et al., 1998) (c) Primitive mantle (PM) normalized La_N vs. Nb_N contents of the JMM to discriminate between hydrothermal and magmatic origin serpentinites. Primitive mantle values are from McDonough and Sun (1995). (d) Geochemical record of interactions between melt/fluid and residues of the JMM serpentinites through Gd/Lu_N vs. Nb_N diagram after Deschamps et al. (2013).

multi-stage history, involving initial high-degree melting to create a refractory residue followed by fluid-mediated metasomatism, is a hallmark of fore-arc mantle evolution. Concurrent MREE–HFSE enrichment trends further reflect superimposed melt/rock and fluid/rock interactions, consistent with global SSZ serpentinites (Fig. 8d). Mantle metasomatism thus involved significant melt–rock interaction (Zhang et al., 2020), while fluid–rock interaction primarily accounts for the HFSE–LREE decoupling (Brenan et al., 1995). However, additional processes are evident: episodic melt addition (via Eu anomalies, variable Zr/Hf), sulfide segregation during refertilization (via PGE fractionation), and a late-stage overprint by slab-derived oxidizing fluids (via selective PGE mobility). This supports a multi-stage SSZ mantle-wedge history involving both melt- and fluid-driven events (Xu & Liu, 2019; Uysal et al., 2025).

The overall low ΣPGE and the flat, depleted nature of the JMM chondrite-normalized PGE patterns (Fig. 7f) are primary magmatic signatures, reflecting the high-degree melting and sulfide exhaustion inferred from major elements (Deschamps et al., 2013). The IPGEs (Os, Ir, Ru) are considered immobile and effectively record this melting event (Pagé et al., 2012). However, the relative enrichment of Pt and Pd over Ir (evident in the average PPGE > IPGE and positive Pd anomalies, Fig. 7f) cannot be explained by melting alone. We interpret this as localized, post-melting, fluid-assisted redistribution of the more mobile PPGEs during serpentinization by oxidizing slab-derived fluids, without significant external PGE addition. This interpretation is supported by the absence of strong correlations between PPGE/IPGE ratios and fluid-mobile elements such as Ba and Sr. This is consistent with studies showing PPGE mobility in hydrous environments (e.g., Marchesi et al., 2014). Although slab-derived fluids have the potential to mobilize Os (Barrett et al., 2022), the internally consistent IPGE patterns observed in our samples suggest that such effects, if present, were minor. The absence of strong correlations between PGE ratios and fluid-mobile element abundances suggests the redistribution was a localized, grain-scale process during fluid infiltration, preserving the primary magmatic PGE depletion signature at the whole-rock scale (Lorand et al., 2013; Becker & Dale, 2016).

5.4. Geodynamic Implications

The JMM serpentinites preserve a record of Neo-Tethyan mantle wedge processes during intra-oceanic subduction initiation. Their highly refractory compositions (Cr# 0.42–0.48; Mg# 0.58–0.61) unequivocally identify them as residues of extensive melt extraction (Deschamps et al., 2013). This high-degree melting signature is further supported by pronounced depletion in incompatible elements, reflected in low whole-rock Th_n and Nb_n values, with Nb_n–Th_n systematics plotting within fields typical of nascent fore-arc and convergent margin settings (Fig. 9a, b; Saccani, 2015). Collectively, these geochemical fingerprints position the JMM as a fragment of the highly depleted, early-stage fore-arc mantle wedge (Fig. 9c; Deschamps et al., 2013; Aldanmaz et al., 2020), formed during subduction initiation prior to intense metasomatic overprinting. This proto-fore-arc lithosphere was subsequently modified within the evolving subduction system. Interaction with slab-derived, oxidizing fluids led to pervasive serpentinization, imprinting the observed LILE enrichment, elevated fO_2, and magnetite formation, a process analogous to the hydration mechanism in fore-arc mantle

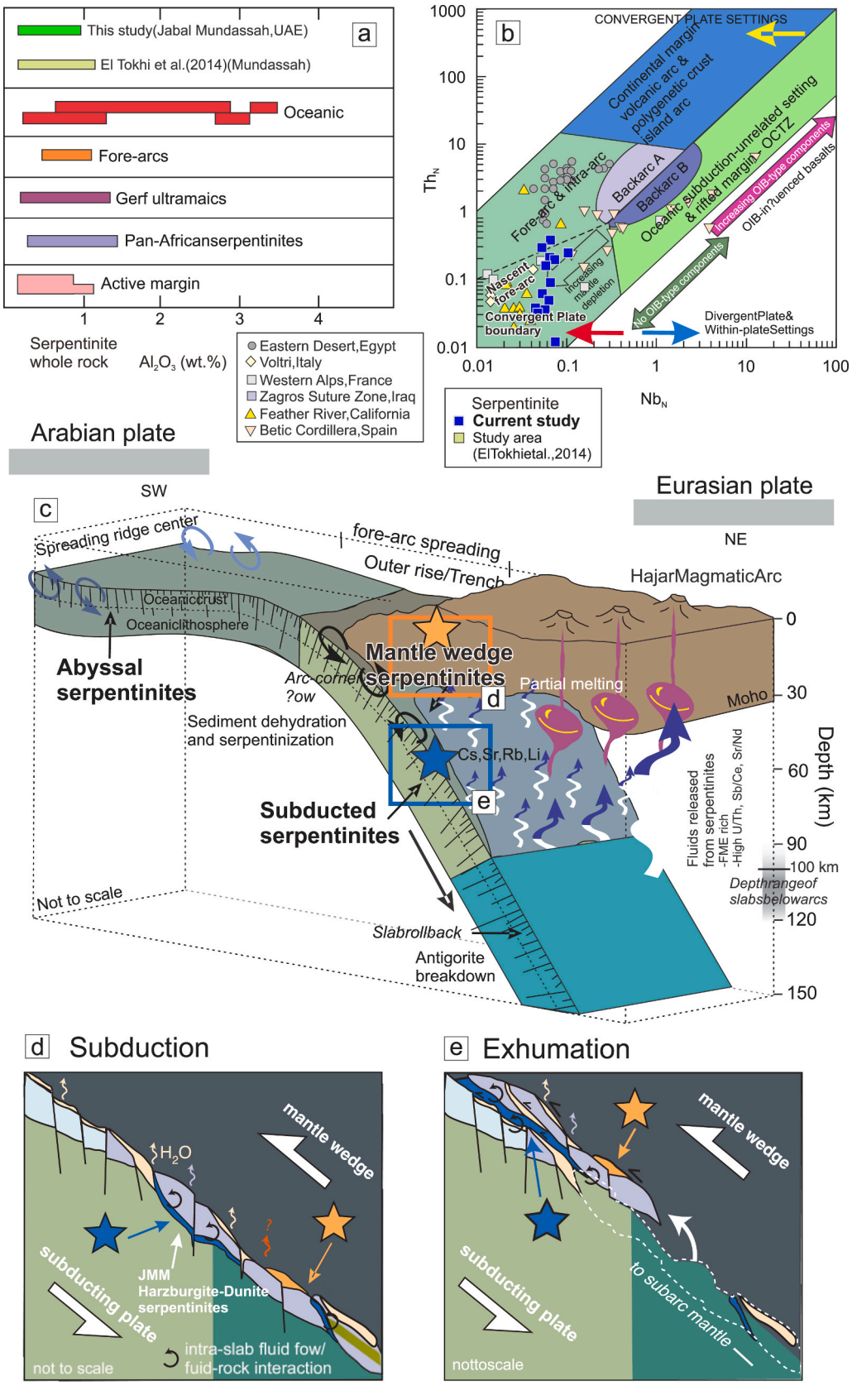

(caption on next page)

Fig. 9. Geodynamic evolution, (a) Whole rock Al_2O_3 contents of the JMM serpentinites compared with those from other tectonic settings (Deschamps et al., 2013), (b) Nb_N vs Th_N tectonic discrimination diagram (after Saccani, 2015), (c) Geodynamic model for the tectonomagmatic evolution of the JMM area in an intra-oceanic environment (modified after Deschamps et al., 2013). The model illustrates the formation of the JMM complex during subduction between the Arabian and Eurasian plates, highlighting subduction-related serpentinization and the geological impact of serpentinites. (d & e) Magnified views of subduction and exhumation processes from Fig. c. (d) Oceanic lithosphere, including serpentinites, is subducted into the mantle, with fluids released from serpentine minerals playing a key role in fluid-rock interactions and potential partial melting in the mantle wedge, (e) Subducted serpentinites, after undergoing high pressure and temperature, are exhumed to the surface through tectonic processes.

wedges (Fig. 9d**;** Deschamps et al., 2013). The JMM lacks the extreme fluid-mobile element (FME) enrichment diagnostic of intense metasomatism at the plate interface. This key distinction indicates it was not fluxed by the deep, channelized fluids released during advanced subduction and metamorphic sole dehydration (Fig. 9c) (Prigent et al., 2018), reinforcing its origin in the overlying mantle wedge rather than the basal shear zone.

The final tectonic emplacement of the JMM fragment onto the Arabian margin is attributed to the Late Cretaceous closure of the Neo-Tethys. During the large-scale obduction of the Semail ophiolite, disparate lithospheric fragments were juxtaposed and accreted (Rioux et al., 2016; Pilia et al., 2021). Thus, we proposed that the JMM likely represents a slice of fore-arc mantle that was mechanically incorporated into the obduction thrust system (Fig. 9e**)**. Its preservation as a less-modified fragment supports models of a laterally heterogeneous ophiolite belt (Searle, 1999) and provides petrological evidence for the multi-stage obduction of fore-arc lithosphere.

6. Conclusion

The Jabal Mundassah–Malaqet (JMM) serpentinites represent a highly refractory mantle residue that preserves an important record of supra-subduction zone processes during the early evolution of the Neo-Tethyan fore-arc. Integrated petrography, X-ray diffraction, mineral chemistry, whole-rock geochemistry, and PGEs systematics demonstrate that these rocks derive from a dunite–harzburgite protolith formed by high-degree melt extraction. This interpretation is supported by their very low Al_2O_3 and TiO_2 contents, high MgO, elevated Mg#, enrichments in compatible elements (Ni, Cr, Co), depleted HFSE and Th–U concentrations, and low total PGE abundances consistent with sulfide exhaustion during extensive melting.

XRD confirmation of coexisting lizardite and antigorite indicates progressive serpentinization under fore-arc conditions. The enrichment of fluid-mobile large-ion lithophile elements (Rb, Sr, Ba and K), together with abundant magnetite and elevated oxygen fugacity inferred from V–MgO systematics, documents overprinting by oxidizing slab-derived fluids. However, the moderate magnitude of this enrichment and the absence of amphibole crystallization indicate that the JMM serpentinites were not affected by the intense, channelized metasomatism that characterizes basal shear zones within the Semail Ophiolite. Instead, they record a more regional fore-arc fluid overprint superimposed on a highly depleted mantle residue.

Cr-spinel compositions (Cr# = 0.42–0.48; Mg# = 0.58–0.61) and PGE fractionation patterns further support formation within a nascent fore-arc mantle wedge and distinguish the JMM fragment from chromite-rich and strongly refertilized domains of the Oman ophiolite. Together, these data indicate a multi-stage evolution involving (i) high-degree melt extraction during intra-oceanic subduction initiation, (ii) subsequent serpentinization and redox modification by slab-derived oxidizing fluids, and (iii) final tectonic emplacement during Late Cretaceous obduction onto the Arabian margin.

The JMM serpentinites therefore provide new constraints on the composition, redox state, and metasomatic architecture of the Neo-Tethyan fore-arc mantle preserved in the eastern UAE. More broadly, this study highlights the strong lateral heterogeneity of fore-arc mantle domains and emphasizes the value of integrated PGE, spinel, and whole-rock geochemical approaches for reconstructing subduction initiation and early fore-arc evolution.

CRediT authorship contribution statement

Mabrouk Sami: Writing – review & editing, Writing – original draft, Validation, Supervision, Resources, Project administration, Methodology, Investigation, Funding acquisition, Formal analysis, Data curation, Conceptualization. **Hamed Gamaleldien:** Writing – review & editing, Visualization, Software, Methodology, Investigation, Formal analysis, Data curation. **Theodoros Ntaflos:** Validation, Supervision, Methodology, Formal analysis, Data curation, Conceptualization. **Chun-Feng Li:** Visualization, Validation, Project administration, Investigation, Data curation, Conceptualization. **Ioan V. Sanislav:** Writing – review & editing, Visualization, Validation, Resources, Methodology, Data curation, Conceptualization. **Xun Zhao:** Writing – review & editing, Validation, Software, Resources, Investigation, Conceptualization. **Vandi Dlama Kamaunji:** Writing – review & editing, Writing – original draft, Software, Resources, Methodology, Investigation, Data curation, Conceptualization. **Bahaa M. Amin:** Validation, Software, Resources, Methodology, Formal analysis, Data curation. **Douaa Fathy:** Writing – original draft, Visualization, Validation, Software, Resources, Investigation, Data curation, Conceptualization. **Mostafa R. Abukhadra:** Writing – review & editing, Software, Formal analysis. **Khaled Abdelfadil:** Writing – review & editing, Validation, Software, Methodology, Investigation, Formal analysis, Data curation. **Suhail S. Alhejji:** Writing – review & editing, Validation, Software, Methodology, Funding acquisition.

Declaration of competing interest

The authors declare that they have no known competing financial interests or personal relationships that could have appeared to influence the work reported in this paper.

Acknowledgement

We appreciate useful comments and advice from two anonymous reviewers and editors which improved the text and data interpretation. The authors express their sincere appreciation to Ahmed Gad for his valuable assistance during the early phases of this research. This study was financially supported by the grants (No G00004879-12S155 and G00004980-12S218) from the United Arab Emirates University, UAE. Sincere thanks and gratitude to the Ongoing Research Funding Program (ORF-2026-1459), King Saud University, Riyadh, Saudi Arabia, for funding this research article. This research was also funded by Khalifa University of Science and Technology through the RIG-2025 under Project ID: KU-INT-RIG-2025-8471000063.

Appendix A. Supplementary data

Supplementary data to this article can be found online at https://doi.org/10.1016/j.jseaes.2026.106990.

Data availability

The data that has been used is confidential.

References

Abd-Allah, A.M., Hashem, W.A., Abdelghany, O., 2013. Structural and tectonostratigraphic evolution of the upper cretaceous–eocene sequence in Malaqet–Mundassah–El Saah range, Oman mountains, United Arab Emirates and Oman. J. Afr. Earth Sci. 79, 111–124.

Abd El-Gawad, E.A., Abdelghany, O., Lotfy, M.A., Hashem, W.A.A., Saima, M., 2010. Basin analysis of the Late Cretaceous Sediments in United Arab Emirates. Aust. J. Basic Appl Sci. 4 (8), 3526–3545.

Abdelfadil, K.M., Asran, A.M., Rehman, H.U., Sami, M., Ahmed, A., Sanislav, I.V., Fnais, M.S., Mogahed, M.M., 2024. The Evolution of Neoproterozoic Mantle Peridotites Beneath the Arabian–Nubian Shield: Evidence from Wadi Sodmein Serpentinites, Central Eastern Desert. Egypt. Minerals 14 (11), 1157.

Andréani, M., Mével, C., Boullier, A.M., Escartin, J., 2007. Dynamic control on serpentine crystallization in veins: Constraints on hydration processes in oceanic peridotites. Geochem. Geophys. Geosyst. 8 (2).

Ague, J.J., 2017. Element mobility during regional metamorphism in crustal and subduction zone environments with a focus on the rare earth elements (REE). Am. Mineral. 102 (9), 1796–1821.

Ahmed, A.H., 2024. Field and petrological characteristics of PGE-rich podiform chromitites: Implications for efficient exploration. J. Asian Earth Sci. 259, 105920.

Ahmed, A., Arai, S., 2002. Unexpectedly high-PGE chromitite from the deeper mantle section of the northern Oman ophiolite and its tectonic implications. Contrib. Mineral. Petrol. 143 (3), 263–278.

Ahmed, A.H., Habtoor, A., 2015. Heterogeneously depleted Precambrian lithosphere deduced from mantle peridotites and associated chromitite deposits of Al'Ays ophiolite, Northwestern Arabian Shield. Saudi Arabia. Ore Geol. Rev. 67, 279–296.

Aldanmaz, E., van Hinsbergen, D.J., Yıldız-Yüksekol, Ö., Schmidt, M.W., McPhee, P.J., Meisel, T., Mason, P.R., 2020. Effects of reactive dissolution of orthopyroxene in producing incompatible element depleted melts and refractory mantle residues during early fore-arc spreading: constraints from ophiolites in eastern Mediterranean. Lithos 360, 105438.

Ali, S., Ntaflos, T., Sami, M., 2021. Geochemistry of Khor Um-Safi ophiolitic serpentinites, central Eastern desert, Egypt: Implications for Neoproterozoic arc-basin system in the Arabian-Nubian shield. Geochemistry 81 (1), 125690.

Arai, S., 1994. Characterization of spinel peridotites by olivine-spinel compositional relationships: review and interpretation. Chem. Geol. 113 (3–4), 191–204.

Arai, S., Miura, M., Tamura, A., Akizawa, N., Ishikawa, A., 2020. Hydrothermal chromitites from the Oman ophiolite: The role of water in chromitite genesis. Minerals 10 (3), 217.

Bach, W., Paulick, H., Garrido, C.J., Ildefonse, B., Meurer, W.P., Humphris, S.E., 2006. Unraveling the sequence of serpentinization reactions: petrography, mineral chemistry, and petrophysics of serpentinites from MAR 15 N (ODP Leg 209, Site 1274). Geophys. Res. Lett. 33 (13).

Barnes, S.J., Roeder, P.L., 2001. The range of spinel compositions in terrestrial mafic and ultramafic rocks. Journal of petrology 42 (12), 2279–2302.

Barrett, N., Jaques, A.L., González-Álvarez, I., Walter, M.J., Pearson, D.G., 2022. Ultra-refractory peridotites of Phanerozoic mantle origin: The Papua New Guinea ophiolite mantle tectonites. J. Petrol. 63 (3), egac014.

Beard, J.S., Frost, B.R., 2017. The stoichiometric effects of ferric iron substitutions in serpentine from microprobe data. Int. Geol. Rev. 59 (5–6), 541–547.

Beard, J.S., Frost, B.R., Fryer, P., McCaig, A., Searle, R., Ildefonse, B., Zinin, P., Sharma, S.K., 2009. Onset and progression of serpentinization and magnetite formation in olivine-rich troctolite from IODP Hole U1309D. J. Petrol. 50 (3), 387–403.

Becker, H., Dale, C.W., 2016. Re–Pt–Os isotopic and highly siderophile element behavior in oceanic and continental mantle tectonites. Rev. Mineral. Geochem. 81 (1), 369–440.

Bhat, I.M., Ahmad, T., Rao, D.S., Balakrishnan, S., Rao, N.C., 2021. PGE and isotopic characteristics of Shergol and Suru Valley ophiolites, Western Ladakh: Implications for supra-subduction tectonics along Indus suture zone: Geosci. Front. 12 (3), 101118.

Brenan, J.M., Shaw, H.F., Ryerson, F.J., Phinney, D.L., 1995. Mineral-aqueous fluid partitioning of trace elements at 900 C and 2.0 GPa: Constraints on the trace element chemistry of mantle and deep crustal fluids. Geochim. Cosmochim. Acta. 59 (16), 3331–3350.

Canil, D., 2002. Vanadium in peridotites, mantle redox and tectonic environments: Archean to present. Earth Planet. Sci. Lett. 195 (1–2), 75–90.

Cannaò, E., Scambelluri, M., Agostini, S., Tonarini, S., Godard, M., 2016. Linking serpentinite geochemistry with tectonic evolution at the subduction plate-interface: The Voltri Massif case study (Ligurian Western Alps, Italy). Geochim. Cosmochim. Acta. 190, 115–133.

Chalot-Prat, F., Ganne, J., Lombard, A., 2003. No significant element transfer from the oceanic plate to the mantle wedge during subduction and exhumation of the Tethys lithosphere (Western Alps). Lithos 69 (3–4), 69–103.

Cocomazzi, G., Grieco, G., Tartarotti, P., Bussolesi, M., Zaccarini, F., Crispini, L., Science Team, O.D.P, 2020. The formation of dunite channels within harzburgite in the Wadi Tayin massif, oman ophiolite: Insights from compositional variability of Cr-spinel and olivine in holes ba1b and ba3a, oman drilling project. Minerals 10 (2), 167.

Deschamps, F., Godard, M., Guillot, S., Hattori, K., 2013. Geochemistry of subduction zone serpentinites: A review. Lithos 178, 96–127.

Dick, H.J., Bullen, T., 1984. Chromian spinel as a petrogenetic indicator in abyssal and alpine-type peridotites and spatially associated lavas. Contrib. Mineral. Petrol. 86, 54–76.

Eickmann, B., Little, C.T., Peckmann, J., Taylor, P.D., Boyce, A.J., Morgan, D.J., Bach, W., 2021. Shallow-marine serpentinization-derived fluid seepage in the Upper Cretaceous Qahlah Formation. United Arab Emirates. Geol. Mag. 158 (9), 1561–1571.

El Tokhi, M., Alaabed, S., Amin, B.E., 2014. Semail Ophiolite supra-subduction zone setting: evidence from serpentinites and their chromite at Mundassah area. UAE. Eur. Sci. J. 10 (24), 364–383.

Evans, B.W., 2004. The serpentinite multisystem revisited: chrysotile is metastable. Int. Geol. Rev. 46 (6), 479–506.

Evans, B.W., Hattori, K., Baronnet, A., 2013. Serpentinite: what, why, where? Elements 9 (2), 99–106.

Evans, K.A., 2012. The redox budget of subduction zones. Earth-Science Reviews 113 (1–2), 11–32.

Farahat, E., Hoinkes, G., Mogessie, A., 2011. Petrogenetic and geotectonic significance of Neoproterozoic suprasubduction mantle as revealed by the Wizer ophiolite complex, Central Eastern Desert. Egypt. Int. J. Earth Sci. 100, 1433–1450.

Faris, M., Abdelghany, O., Saima, M.A., 2012. Upper Cretaceous to Lower Eocene calcareous nannofossil biostratigraphy from Malaqet and Mundassah sections western flank of the Northern Oman Mountains. Geol. Croat. 65 (3), 393–410.

Gamal El Dien, H., Arai, S., Doucet, L.S., Li, Z.X., Kil, Y., Fougerouse, D., Hamdy, M., 2019. Cr-spinel records metasomatism not petrogenesis of mantle rocks. Nat. Commun. 10 (1), 5103.

Garrido, C.J., López Sánchez-Vizcaíno, V., Gómez-Pugnaire, M.T., Trommsdorff, V., Alard, O., Bodinier, J.L., Godard, M., 2005. Enrichment of HFSE in chlorite-harzburgite produced by high-pressure dehydration of antigorite-serpentinite: Implications for subduction magmatism. Geochem. Geophys. Geosyst. 6 (1).

Garuti, G., Fershtater, G., Bea, F., Montero, P., Pushkarev, E.V., Zaccarini, F., 1997. Platinum-group elements as petrological indicators in mafic-ultramafic complexes of the central and southern Urals: preliminary results. Tectonophysics 276, 181–194.

Godard, M., Jousselin, D., Bodinier, J.L., 2000. Relationships between geochemistry and structure beneath a palaeo-spreading centre: a study of the mantle section in the Oman ophiolite. Earth Planet. Sci. Lett. 180 (1–2), 133–148.

Gruau, G., Bernard-Griffiths, J., Lécuyer, C., 1998. The origin of U-shaped rare earth patterns in ophiolite peridotites: assessing the role of secondary alteration and melt/rock reaction. Geochim. Cosmochim. Acta 62 (21/22), 3545–3560.

Hanghøj, K., Kelemen, P.B., Hassler, D., Godard, M., 2010. Composition and genesis of depleted mantle peridotites from the Wadi Tayin Massif, Oman Ophiolite; major and trace element geochemistry, and Os isotope and PGE systematics. J. Petrol. 51 (1–2), 201–227.

Hart, S.R., Zindler, A., 1986. In search of a bulk-Earth composition. Chem. Geol. 57 (3–4), 247–267.

Hilairet, N., Daniel, I., Reynard, B., 2006. Equation of state of antigorite, stability field of serpentines, and seismicity in subduction zones. Geophys. Res. Lett. 33 (2).

Ishii, T., Robinson, P.T., Maekawa, H., Fiske, R., 1992. Petrological studies of peridotites from diapiric serpentinite seamounts in the izu- ogasawara-Mariana forearc, leg 125. In: Pearce, J., Stokking, L.B., al, et (Eds.), Proceedings of the Ocean Drilling Project, Leg 125, Scientific Results (College Station), pp. 445–485.

Ismail, S.A., Mirza, T.M., Carr, P.F., 2010. Platinum-group elements geochemistry in podiform chromitites and associated peridotites of the Mawat ophiolite, northeastern Iraq. J. Asian Earth Sci. 37 (1), 31–41.

Jabir, M.A., Ali, M.Y., Ismaiel, M., Watts, A.B., 2023. Subsidence and uplift history of the UAE and the western flank of the UAE-Oman mountain range. Tectonics 42 (10), e2023TC007998.

Kamenetsky, V.S., Crawford, A.J., Meffre, S., 2001. Factors controlling chemistry of magmatic spinel: an empirical study of associated olivine, Cr-spinel and melt inclusions from primitive rocks. J. Petrol. 42 (4), 655–671.

Kapsiotis, A., Grammatikopoulos, T.A., Tsikouras, B., Hatzipanagiotou, K., Zaccarini, F., Garuti, G., 2009. Chromian Spinel Composition and Platinum-Group Element Mineralogy of Chromitites from The Milia Area, Pindos Ophiolite Complex. Greece. Can. Mineral. 47, 1037–1056.

Kelley, K.A., Cottrell, E., 2009. Water and the oxidation state of subduction zone magmas. Science 325 (5940), 605–607.

Khedr , M.Z. , Arai , S. , 2017 Peridotite-chromitite complexes in the Eastern Desert of Egypt: Insight into Neoproterozoic sub-arc mantle processes. Gondwana Res. 52, 59–79.

Kodolányi, J., Pettke, T., Spandler, C., Kamber, B.S., Gméling, K., 2012. Geochemistry of ocean floor and fore-arc serpentinites: constraints on the ultramafic input to subduction zones. Journal of Petrology 53 (2), 235–270.

Le Maitre, R.W. (Ed.), 2002. Igneous Rocks. A Classification and Glossary of Terms. Recommendations of the International Union of Geological Sciences Subcommission on the Systematics of Igneous Rocks, 2nd edition, 140(3), xvi + 236 pp. Cambridge University Press, Cambridge, New York, Melbourne.

Lee, C.T.A., Brandon, A.D., Norman, M., 2003. Vanadium in peridotites as a proxy of Paleo-$fO2$ during partial melting: prospects, limitations and implications. Geochim. Cosmochim. Acta. 67, 3045–3064.

Li, K., Wu, K., Yu, A.J., Du, Y.F., Sun, W., Li, L., 2025. Mantle wedge serpentinites as a potential nitrogen reservoir regulating subduction-zone nitrogen recycling and mantle heterogeneity. Earth and Planetary Science Letters 653, 119211.

Li, Z.X.A., Lee, C.T.A., 2006. Geochemical investigation of serpentinized oceanic lithospheric mantle in the Feather River Ophiolite, California: implications for the recycling rate of water by subduction. Chem. Geol. 235 (1–2), 161–185.

Lorand, J.P., Luguet, A., Alard, O., 2013. Platinum-group element systematics and petrogenetic processing of the continental upper mantle: A review. Lithos 164, 2–21.

Maier, W.D., Roelofse, F., Barnes, S.J., 2003. The concentration of the platinum-group elements in South African komatiites: implications for mantle sources, melting regime and PGE fractionation during crystallization. J. Petrol. 44 (10), 1787–1804.

Mallmann, G., O'Neill, H.S.C., 2009. The crystal/melt partitioning of V during mantle melting as a function of oxygen fugacity compared with some other elements (Al, P, Ca, Sc, Ti, Cr, Fe, Ga, Y, Zr and Nb). J. Petrol. 50 (9), 1765–1794.
Marchesi, C., Dale, C.W., Garrido, C.J., Pearson, D.G., Bosch, D., Bodinier, J.L., Hidas, K., 2014. Fractionation of highly siderophile elements in refertilized mantle: Implications for the Os isotope composition of basalts. Earth Planet. Sci. Lett. 400, 33–44.
McDonough, W.F., Sun, S.S., 1995. The composition of the Earth. Chem. Geol. 120 (3–4), 223–253.
Melcher, F., Grum, W., Thalhammer, T.V., Thalhammer, O.A.R., 1999. The giant chromite deposits at Kempirsai, Urals: constraints from trace element (PGE, REE) and isotope data. Mineralium Deposita 34, 250–272.
Mével, C., 2003. Serpentinization of abyssal peridotites at mid-ocean ridges. C. R. - Geosci. 335 (10–11), 825–852.
Nicolas, A., Boudier, F., Ildefonse, B., Ball, E., 2000. Accretion of Oman and United Arab Emirates ophiolite–Discussion of a new structural map. Mar. Geophys. Res. 21 (3), 147–180.
Modjarrad, M., Whitney, D.L., Omrani, H., 2024. Petrologic evolution of the Gysian ophiolitic serpentinites. NW Iran. Acta Geochim. 43 (5), 996–1011.
Modjarrad, M., Uysal, I., Moghadam, H.S., Demir, Y., Müller, D., 2025. Geochemical insights and petrogenetic processes of ophiolitic fragments from Avajiq and Silvana: implications for Neo-Tethyan Evolution in northwest Iran. Int. Geol. Rev. 67, 1437–1465.
Monsef, I., Monsef, R., Mata, J., Zhang, Z., Pirouz, M., Rezaeian, M., Esmaeili, R., Xiao, W., 2018. Evidence for an early-MORB to fore-arc evolution within the Zagros suture zone: Constraints from zircon U-Pb geochronology and geochemistry of the Neyriz ophiolite (South Iran). Gondwana Res. 62, 287–305.
Niu, Y., 2004. Bulk-rock major and trace element compositions of abyssal peridotites: implications for mantle melting, melt extraction and post-melting processes beneath mid-ocean ridges. J. Petrol. 45, 2423–2458.
Norris, A., Danyushevsky, L., 2018. Towards Estimating the Complete Uncertainty Budget of Quantified Results Measured by LA-ICP-MS. Goldschmidt, Boston.
Ohara, Y., Ishii, T., 1998. Peridotites from the southern Mariana forearc: Heterogeneous fluid supply in mantle wedge. Isl. Arc 7, 541–558.
Pagé, P., Barnes, S.J., Bédard, J.H., Zientek, M.L., 2012. In situ determination of Os, Ir, and Ru in chromites formed from komatiite, tholeiite and boninite magmas: implications for chromite control of Os, Ir and Ru during partial melting and crystal fractionation. Chem. Geol. 302, 3–15.
Parkinson, I.J., Pearce, J.A., 1998. Peridotites from the Izu–Bonin–Mariana forearc (ODP Leg 125): evidence for mantle melting and melt–mantle interaction in a supra-subduction zone setting. J. Petrol. 39 (9), 1577–1618.
Paulick, H., Bach, W., Godard, M., De Hoog, J.C.M., Suhr, G., Harvey, J., 2006. Geochemistry of abyssal peridotites (Mid-Atlantic Ridge, 15∘20′N, ODP Leg 209): Implications for fluid/rock interaction in slow spreading environments. Chem. Geol. 234, 179–210.
Pearce, J.A., 1982. Trace element characteristics of lavas from destructive plate boundaries. Orogenic andesites and related rocks 528–548.
Pearce, J.A., Lippard, S.J., Roberts, S., 1984. In: Kokelaar, B.P., Howells, M.F. (Eds.), Characteristics and Tectonic Significance of Supra-Subduction Ophiolites, 16. Geol. Soc. Spec. Publ. 777–794.
Pearce, J.A., Barker, P., Edwards, S., Parkinson, I., Leat, P., 2000. Geochemistry and tectonic significance of peridotites from the South Sandwich arc–basin system, South Atlantic. Contrib. Mineral. Petrol. 139, 36–53.
Pearce, J.A., Stern, R.J., 2006. Origin of back-arc basin magmas: Trace element and isotope perspectives. Back-arc spreading systems: Geological, biological, chemical, and physical interactions 166, 63–86.
Pilia, S., Kaviani, A., Searle, M.P., Arroucau, P., Ali, M.Y., Watts, A.B., 2021. Crustal and mantle deformation inherited from obduction of the Semail ophiolite (Oman) and continental collision (Zagros). Tectonics 40 (6), e2020TC006644.
Prigent, C., Agard, P., Guillot, S., Godard, M., Dubacq, B., 2018. Mantle wedge (de) formation during subduction infancy: Evidence from the base of the Semail ophiolitic mantle. J. Petrol. 59 (11), 2061–2092.
Prytulak, J., Nielsen, S.G., Ionov, D.A., Halliday, A.N., Harvey, J., Kelley, K.A., Niu, Y.L., Peate, D.W., Shimizu, K., Sims, K.W.W., 2013. The stable vanadium isotope composition of the mantle and mafic lavas. Earth Planet. Sci. Lett. 365, 177–189.
Rioux, M., Garber, J., Bauer, A., Bowring, S., Searle, M., Kelemen, P., Hacker, B., 2016. Synchronous formation of the metamorphic sole and igneous crust of the Semail ophiolite: New constraints on the tectonic evolution during ophiolite formation from high-precision U–Pb zircon geochronology. Earth Planet. Sci. Lett. 451, 185–195.
Rollinson, H., 2017. Masirah–the other Oman ophiolite: A better analogue for mid-ocean ridge processes? Geosci. Front.] 8 (6), 1253–1262.
Saccani, E., 2015. A new method of discriminating different types of post-Archean ophiolitic basalts and their tectonic significance using Th-Nb and Ce-Dy-Yb systematics. Geosci. Front. 6 (4), 481–501.
Saha, A., Santosh, M., Ganguly, S., Manikyamba, C., Ray, J., Dutta, J., 2018. Geochemical cycling during subduction initiation: Evidence from serpentinized mantle wedge peridotite in the south Andaman ophiolite suite. Geosci Front. 9 (6), 1755–1775.
Saibi, H., Hag, D.B., Alamri, M.S.M., Ali, H.A., 2021. Subsurface structure investigation of the United Arab Emirates using gravity data. Open Geosci 13 (1), 262–271.
Scambelluri, M., Cannaò, E., Gilio, M., 2019. The water and fluid-mobile element cycles during serpentinite subduction. A review. Eur. J. Mineral. 31 (3), 405–428.
Schmidt, A., Weyer, S., John, T., Brey, G.P., 2009. HFSE systematics of rutile-bearing eclogites: new insights into subduction zone processes and implications for the earth's HFSE budget. Geochim. Cosmochim. Acta. 73 (2), 455–468.
Searle, M., 2019. Ophiolites and structure of the Oman – UAE mountains. Searle, Geology of the Oman Mountains, Eastern Arabia. Springer, Cham, In M, p. 478p.
Searle, M., Cox, J., 1999. Tectonic setting, origin, and obduction of the Oman ophiolite. Geol. Soc. Am. Bull. 111(1), 104–122.
Sharma, M., Wasserburg, G.J., 1996. The neodymium isotopic compositions and rare earth patterns in highly depleted ultramafic rocks. Geochim. Cosmochim. Acta 60, 4537–4550.
Singh, A.K., 2013. Petrology and geochemistry of Abyssal Peridotites from the Manipur Ophiolite Complex, Indo-Myanmar Orogenic Belt, Northeast India: implication for melt generation in mid-oceanic ridge environment. J. Asian Earth Sci. 66, 258–276.
Stern, R.J., Johnson, P., 2010. Continental lithosphere of the Arabian Plate: a geologic, petrologic, and geophysical synthesis. Earth-Sci. Rev. 101 (1–2), 29–67.
Streckeisen, A., 1976. To each plutonic rock its proper name. Earth-Sci. Rev. 12 (1), 1–33.
Taylor, S.R., McLennan, S.M., 1985. The Continental Crust: Its Composition and Evolution. Blackwell, Oxford, pp. 1–312.
Ulrich, M., Muñoz, M., Boulvais, P., Cathelineau, M., Cluzel, D., Guillot, S., Picard, C., 2020. Serpentinization of New Caledonia peridotites: from depth to (sub-) surface. Contrib. Mineral. Petrol. 175, 1–25.
Uysal, I., Tarkian, M., Sadiklar, M.B., Zaccarini, F., Meisel, T., Garuti, G., Heidrich, S., 2009. Petrology of Al-and Cr-rich ophiolitic chromitites from the Muğla, SW Turkey: implications from composition of chromite, solid inclusions of platinum-group mineral, silicate, and base-metal mineral, and Os-isotope geochemistry. Contrib. Mineral. Petrol. 158, 659–674.
Uysal, I., Şen, A.D., Su, B.X., Ersoy, Y., Demir, Y., Pan, Q.Q., Godard, M., 2025. Multiple Mantle Melting and Metasomatism during the Initial Stages of Subduction: Multi-Geochemical and Os-Isotope Evidence from Well-Preserved Kızıldağ Ophiolite, southern Türkiye. J. Petrol. 66 (8), egaf066.
Viti, C., Mellini, M., 1998. Mesh textures and bastites in the Elba retrograde serpentinites. Eur. J. Mineral. 10 (6), 1341–1359.
Wicks, F.J., 1979. Plant, A. Electron microprobe and X-ray microbeam studies of serpentine textures. Can. Mineral. 17, 785–830.
Xu, Y., Liu, C.Z., 2019. Subduction-induced fractionated highly siderophile element patterns in forearc mantle. Minerals 9 (6), 339.
Xu, Y., Liu, J., Xiong, Q., Su, B.X., Scott, J.M., Xu, B., Zhu, D.C., Pearson, D.G., 2020. The complex life cycle of oceanic lithosphere: A study of yarlung-zangbo ophiolitic peridotites, Tibet: Geochim. Cosmochim. Acta. 277, 175–191.
Yin, Z.Z., Chen, R.X., Gong, B., Zha, X.P., 2024. Multiple crust-mantle interactions during tectonic development from oceanic subduction to continental collision: Constraints from mantle wedge serpentinites in a continental subduction zone. Lithos 482, 107713.
Zaccarini, F., Economou-Eliopoulos, M., Kiseleva, O., Garuti, G., Tsikouras, B., Pushkarev, E., Idrus, A., 2022. Platinum Group Elements (PGE) Geochemistry and Mineralogy of Low Economic Potential (Rh-Pt-Pd)-Rich Chromitites from Ophiolite Complexes. Minerals 12 (12), 1565.
Zafar, T., Ur Rehman, H., Maqbool Bhat, I., Ullah, Z., Farhan, M., Oyebamiji, A., Nouri, F., Spedibar, F., Song, S., Hussain, Z., Ali, M., Leng, C., Li, C., Ahmed, M.S., Sami, M., 2024. Exploring the tectono-magmatic evolution of intraoceanic fore-arc setting during subduction initiation: perspectives from trace and platinum group element systematics of the Jijal ultramafic arc system. NE Pakistan. Int. Geol. Rev. 66 (17), 3116–3140.
Zhang, L., Sun, W.D., Zhang, Z.F., An, Y., Liu, F., 2020. Iron Isotope Behavior During Melt-Peridotite Interaction in Supra-subduction Zone Ophiolite From Northern Tibet. J. Geophys. Res. Solid Earth. 125, e2019JB018823.
Zhang, Y., Gazel, E., Gaetani, G.A., Klein, F., 2021. Serpentinite-derived slab fluids control the oxidation state of the subarc mantle. Sci. Adv. 7 (48), eabj2515.